



HAL
open science

Geodetic mass balance of Mýrdalsjökull ice cap, 1999–2021: DEM processing and climate analysis

Maud Bernat

► **To cite this version:**

Maud Bernat. Geodetic mass balance of Mýrdalsjökull ice cap, 1999–2021: DEM processing and climate analysis. *Glaciology*. 2022. dumas-03772002

HAL Id: dumas-03772002

<https://dumas.ccsd.cnrs.fr/dumas-03772002>

Submitted on 7 Sep 2022

HAL is a multi-disciplinary open access archive for the deposit and dissemination of scientific research documents, whether they are published or not. The documents may come from teaching and research institutions in France or abroad, or from public or private research centers.

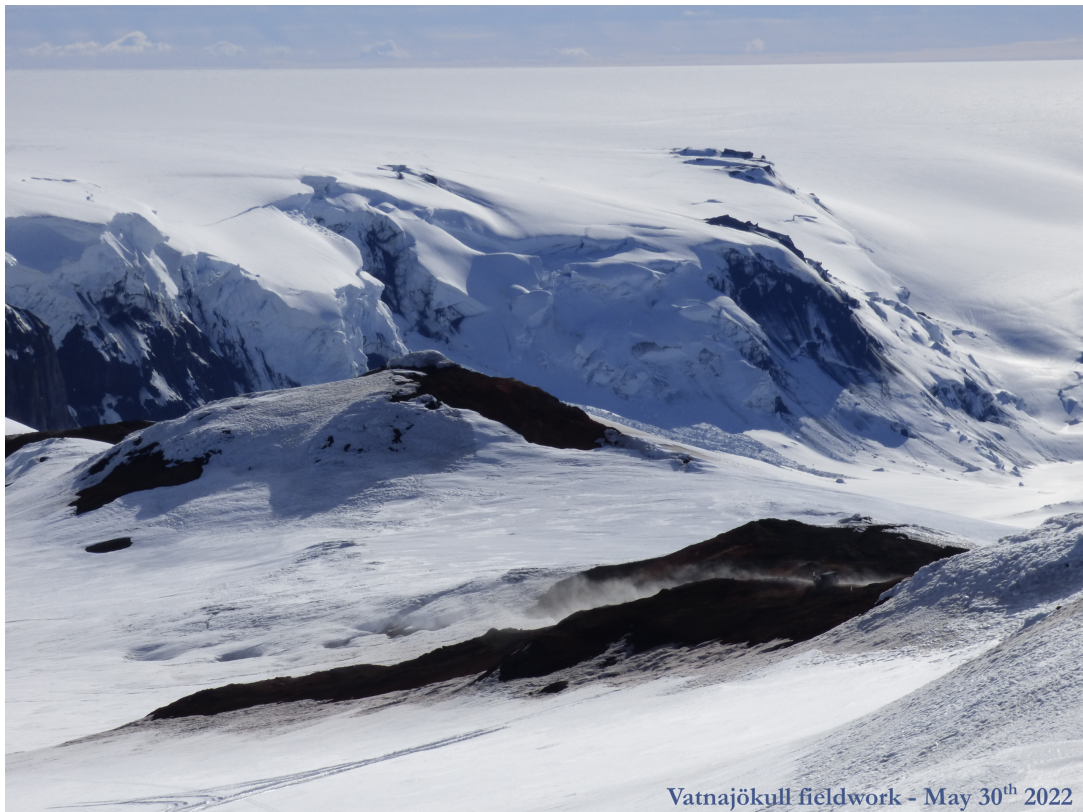
L'archive ouverte pluridisciplinaire **HAL**, est destinée au dépôt et à la diffusion de documents scientifiques de niveau recherche, publiés ou non, émanant des établissements d'enseignement et de recherche français ou étrangers, des laboratoires publics ou privés.

Geodetic mass balance of Mýrdalsjökull ice cap, 1999–2021: DEM processing and climate analysis

Maud BERNAT,

under the supervision of Joaquin MC BELART,

in collaboration with Etienne BERTHIER, Tómas JÓHANNESSEN and Andri GUNNARSSON



Master's internship report

April - September 2022

Abstract

Mýrdalsjökull is the fourth largest Icelandic ice cap ($\sim 480 \text{ km}^2$ in 2019), located in the South of Iceland. Until now, the majority of mass balance studies in Iceland have been centered on the three main Icelandic ice caps. Thus, mass balance estimates of Mýrdalsjökull are scarce. The untapped SPOT5 archive (2002–2015), the lidar data, the Pleiades imagery (2011–present), aerial photographs from 1999 and the ArcticDEM dataset (2010–2019) were used in this study to create Digital Elevation Models (DEMs) of Mýrdalsjökull ice cap. A pre-processing of the DEMs was first performed: co-registration, filtering and interpolation. Then, applying a Gaussian Process regression (GP), a state-of-the-art method in DEM processing, a spatially and temporally continuous DEM dataset was created, in $15 \text{ m} \times 15 \text{ m}$ resolution and 30-day interval from 1999 to 2021. Volume and mass changes based on the synthetic GP-generated DEMs were computed and analyzed in 5-year intervals between 1999 and 2019. A mass loss of $-1.23 \pm 0.10 \text{ m w.e. a}^{-1}$ was observed during this time span. Mass balance showed an increasing trend from $-1.82 \pm 0.16 \text{ m w.e. a}^{-1}$ (1999–2004) to $-0.39 \pm 0.03 \text{ m w.e. a}^{-1}$ (2014–2019). Glaciological mass balance computed annually showed less negative mass balance around 2014–2017, followed by another strong decline after 2017. A local analysis of three glacierized catchments of Mýrdalsjökull was performed. The northern catchment presented the most negative mass balance ($-1.56 \pm 0.16 \text{ m w.e. a}^{-1}$ (1999–2019)). No significant variability in mass balance was observed between the catchments, despite noticeable differences in their climatic conditions. The relationship between glacier mass balance and climatic variations was investigated using a simplified linear model of mass balance forced by climate. A mass balance sensitivity to summer temperature of $-1.35 \text{ m w.e. a}^{-1}\text{K}^{-1}$ was obtained for Mýrdalsjökull, in agreement with the high mass balance sensitivity to temperature changes characteristic of maritime glaciers.

Résumé

Mýrdalsjökull, située dans le Sud de l’Islande, est la quatrième calotte glaciaire islandaise en termes de surface ($\sim 480 \text{ km}^2$ en 2019). Jusqu’à présent, la majorité des études de bilan de masse glaciaire en Islande se sont concentrées sur les trois calottes principales du pays. Les estimations des évolutions de Mýrdalsjökull sont par conséquent assez sporadiques. L’archive de données SPOT5 (2002–2015), encore inexploitée, l’imagerie stéréo Pléiades (2011–présent), les données lidar, des photographies aériennes de 1999 ainsi que les données ArcticDEM ont été utilisées dans cette étude afin de créer des Modèles Numériques de Terrain (MNTs) de la calotte glaciaire Mýrdalsjökull. Un pré-traitement des MNTs a d’abord été effectué: recalage, filtrage et interpolation. Par la suite, une régression par Processus Gaussiens, méthode de pointe du traitement des MNTs, a été appliquée pour créer un ensemble de MNTs spatialement et temporellement continu, avec une résolution spatiale de $15 \text{ m} \times 15 \text{ m}$ et temporelle de 30 jours. En utilisant les MNTs synthétiques générés par les Processus Gaussiens, les changements de volume et de masse ont été calculés sur la période 1999–2019. La perte de masse est estimée à $-1.23 \pm 0.10 \text{ m w.e. a}^{-1}$ sur cet intervalle temporel. Les bilans de masse, calculés sur des périodes de 5 années hydrologiques, présentent une tendance à la hausse, partant de $-1.82 \pm 0.16 \text{ m w.e. a}^{-1}$ (1999–2004) jusqu’à atteindre $-0.39 \pm 0.03 \text{ m w.e. a}^{-1}$ (2014–2019). Les bilans de masse glaciaires calculés annuellement indiquent des valeurs moins négatives autour de 2014–2017, auxquelles succède un fort déclin après 2017. Une analyse locale de trois bassins versants glaciaires a été menée. Le bilan de masse le plus négatif est observé dans le bassin versant glaciaire du Nord ($-1.56 \pm 0.16 \text{ m w.e. a}^{-1}$ (1999–2019)). Malgré des différences notables en termes de conditions climatiques, les trois bassins versants glaciaires présentent une variabilité de bilan de masse similaire. Dans le but d’examiner les relations entre les variations des paramètres climatiques et l’évolution du glacier, un modèle linéaire simplifié de forçage climatique du bilan de masse glaciaire a été appliqué. La sensibilité du bilan de masse aux variations de la température estivale obtenue est de $-1.35 \text{ m w.e. a}^{-1}\text{K}^{-1}$ pour Mýrdalsjökull, en accord les valeurs élevées caractéristiques des glaciers maritimes.

Contents

1	Introduction	2
2	Study region and datasets	3
2.1	Study region	3
2.2	Sources of elevation data	5
2.2.1	Optical stereo imagery: SPOT5 & Pléiades	5
2.2.2	Airborne lidar pointclouds	6
2.2.3	ArcticDEM dataset	6
2.2.4	Aerial photogrammetry	6
2.2.5	ASTER–ArcticDEM elevation change maps	7
2.3	Outlines and ELA	7
2.4	Climatic data	7
3	Methods	7
3.1	Creating elevation difference maps	7
3.1.1	DEM generation	7
3.1.2	DEM co-registration	7
3.1.3	Filtering	8
3.1.4	Elevation difference computation	10
3.1.5	Interpolation	10
3.1.6	Gaussian Process regression	12
3.2	Mass balance computation	13
3.2.1	Volume change and mass balance	13
3.2.2	Uncertainties	14
3.3	Climate analysis	15
3.3.1	Temperature and precipitation data processing	15
3.3.2	Linear model of climate forcing	15
4	Results	16
4.1	Elevation time series	16
4.2	Geodetic mass balance	17
4.3	Catchment scale analysis	18
4.4	Climate model results	19
5	Discussion	21
5.1	Gaussian Process regression	21
5.2	Mass balance	23
5.2.1	Annual mass balance and conversion factor	23
5.2.2	Comparison with other studies	23
5.2.3	Mass balance at the different catchments	24
5.3	Joint analysis of mass balance and climate	25
5.3.1	Climatic sensitivities	25
5.3.2	Linear model limitations	25
6	Conclusion	26

1 Introduction

Glaciers are retreating worldwide and mass-loss rates have accelerated in response to global warming over the past decades. This process affects the environment in many ways, from changing the hydrology to increasing natural hazards and rising sea-level. The contribution of glaciers to global mean sea-level rise was estimated to be 27 ± 22 mm from 1961 to 2016 (Zemp et al., 2019). Between 2000 and 2019,

the global glacier mass loss was assessed as 267 ± 16 Gt per year, which corresponds to $21 \pm 3\%$ of the observed sea-level rise (Hugonnet et al., 2021). In order to investigate the relationship between glacier evolution and climate and better predict future changes, spatially and temporally detailed measurements must be carried out.

Mass balance is widely used in glaciological studies to evaluate glacier changes. The traditional approach consists of conducting regular in situ observations, commonly known as glaciological mass balance (Cogley, 2011). Winter accumulation and summer melting are measured and analysed to obtain annual surface mass balance. However, this requires complex and costly field work. Only a small number of accessible glaciers worldwide can be investigated. Therefore, remote sensing methods have become widely used over the past decades in glaciological research. By comparing surface topography at different times, glacier elevation and volume changes can be quantified and investigated. Digital Elevation Models (DEMs), created from spaceborne and airborne platforms, give a representation of glacier topography that can be used for geodetic mass balance estimates, as tested and validated in various studies (Berthier et al., 2014; Belart et al., 2020). Many space-borne sensors have been launched since the early 2000s and remote sensing observations are now numerous, including publicly available data. The increasing amount of high-resolution datasets enables to create a global picture of glacier mass loss.

Temperate glaciers cover 10% of the area of Iceland (Björnsson and Pálsson, 2008), and represent a volume of ~ 3400 km³ in 2019 (Aðalgeirsdóttir et al., 2020) corresponding to a potential sea-level rise of 9 mm if melted. Icelandic ice caps are characterized by a large variability on decadal time scales related to climate variations and to a lesser extent, to volcanic activity. Despite intermittent periods of close to zero mass balance as in 1970s–1980s, Icelandic glaciers have been retreating since the end of the Little Ice Age around 1890. The total mass loss during this period was estimated to be -540 ± 130 Gt (Aðalgeirsdóttir et al., 2020), half of it happening during the last two and a half decades. The accelerated retreat of Icelandic glaciers also leads to a variety of impacts on water resources, hydropower and tourism.

In Iceland, the three largest ice caps: Vatnajökull, Hofsjökull and Langjökull represent 90% of the glacierized area (Aðalgeirsdóttir et al., 2020). Consequently, most of the glaciological studies have been focused on those glaciers. Glaciological mass balance measurements have been carried out seasonally for ~ 25 years (Björnsson and Pálsson, 2008) and numerous remote sensing studies have been looking at changes of Vatnajökull (e.g. Hannesdóttir et al. (2015)), Hofsjökull (e.g. Aðalgeirsdóttir et al. (2006)) and Langsjökull (e.g. Pálsson et al. (2012)). In the case of Mýrdalsjökull, in situ observations are scarce (Ágústsson et al., 2013) and do not allow the reconstruction of annual mass balance. Thus, estimates of this ice cap changes have rarely been made. Belart et al. (2020) offers an overview of mass balance from 1960 to 2010 in decadal time spans. However, this temporal sampling does not allow to capture variability at shorter spatial or temporal scales. The untapped high precision SPOT5 and Pléiades datasets covering Mýrdalsjökull over the past two decades therefore provide an opportunity to analyse the changes of this ice cap.

The goal of this study is to process high resolution DEMs using state-of-the-art methods in order to produce geodetic mass balance estimates of Mýrdalsjökull in 1999–2021. Those results are used to quantify and analyse spatial and temporal trends and variability of the mass balance. The relationship between mass balance and climate is then investigated through a temperature and precipitation sensitivity study.

2 Study region and datasets

2.1 Study region

Mýrdalsjökull is the fourth largest Icelandic ice cap and covered an area of 480 km² in 2019 (Hannesdóttir et al., 2020). The total volume and average thickness in 2000 were estimated as ~ 140 km³ and ~ 230 m respectively (Björnsson et al., 2000; Björnsson and Pálsson, 2008). Located 15 km North of the South coast of Iceland, the glacier is exposed to a maritime climate. Extratropical lows that recurrently hit the South make this region the wettest in Iceland (Crochet, 2007). In winter, Mýrdalsjökull receives around 6–9 m of precipitation (Fig. 1c) and the annual total can exceed 10 m.

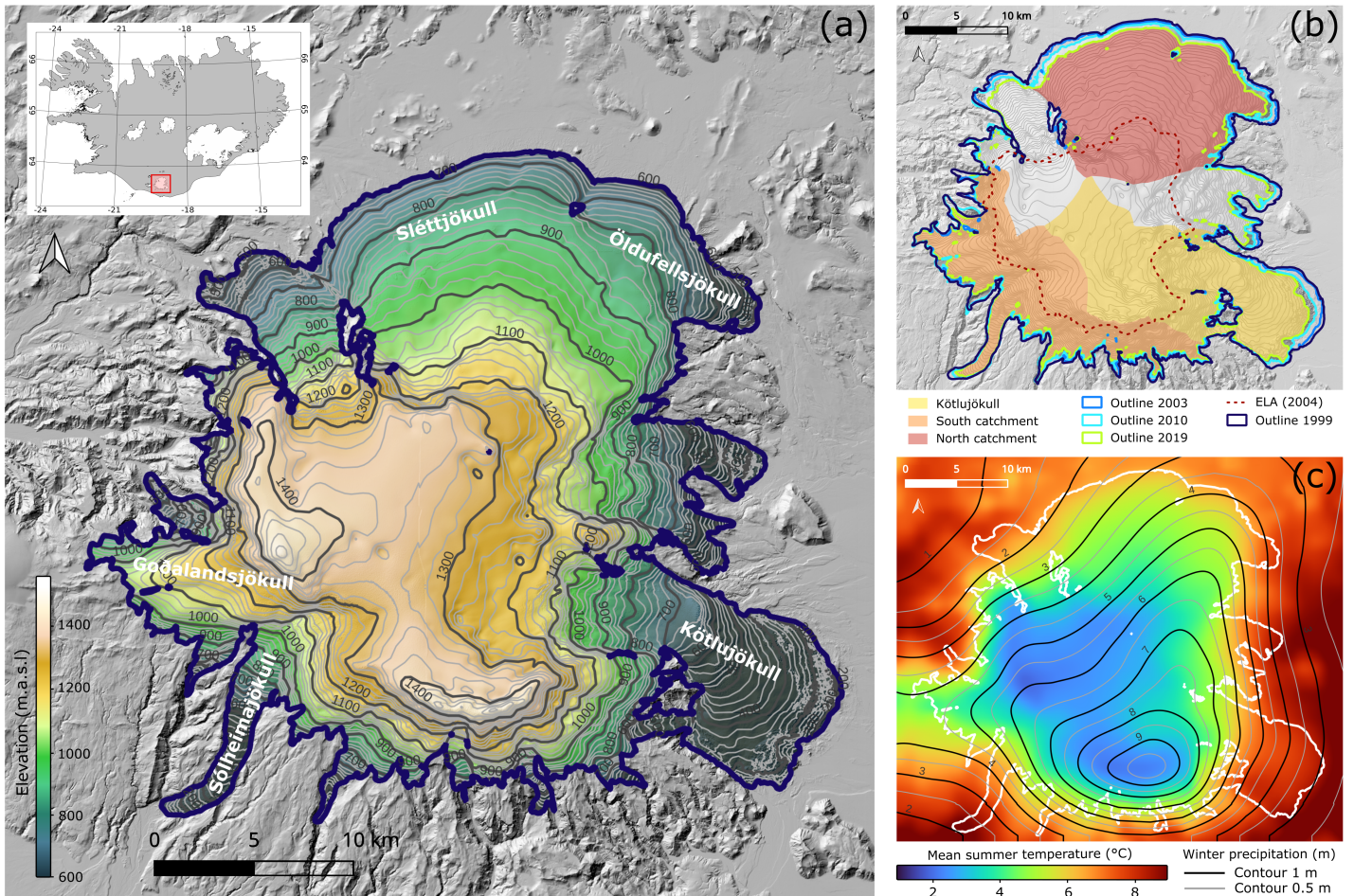


Fig. 1: (a) DEM of Mýrdalsjökull from IslandsDEM and corresponding contour map (contour interval of 100 m in black, 20 m in grey). The names of the main outlets are indicated in white. (b) Mýrdalsjökull glacier outlines in 1999, 2003, 2010 and 2019 and definition of the main glacierized catchments (North, South and Kötlujökull). The Equilibrium Line Altitude (ELA) derived from a 2004-10-05 SPOT5 orthoimage (Belart et al., 2020) is indicated as a red dashed line. (c) Average climatic conditions between 1999 and 2019: mean summer temperature is shown in the background, total winter precipitation in meters is displayed as contours in meters per year.

The orographic uplift of the impinging airflow caused by the surrounding mountains also participates in the high precipitation rates in this area.

The ice cap topography rises from 200 m up to 1480 m (Fig. 1a). The largest part of the accumulation area is a gently sloping plateau between 1300 m and 1350 m.a.s.l. It is surrounded by nunataks emerging 100 m to 200 m above the central zone. Further away, several outlets including Sléttjökull and Öldufellsjökull in the North, Kötlujökull in the Southeast and Sólheimajökull and Goðalandsjökull in the Southwest, are fed by the accumulation area. The moderate elevation of Mýrdalsjökull compared to the other Icelandic ice caps leads to higher temperatures on average. During summer, the temperature goes far above 0°C (Fig. 1c), causing high summer melting rates.

An active volcano named Katla is located under Mýrdalsjökull. The caldera covers a roughly circular area of $\sim 100 \text{ km}^2$ under the central part of the glacier. The eruption frequency is estimated to be around once every 40 to 80 years (Gudmundsson et al., 2008). No eruption has taken place since the last one in 1918. However, the induced geothermal activity is clearly visible through the appearing and disappearing of geothermal cauldrons at many locations on the glacier. The geothermal heating has also been the source of regular jökulhlaups affecting a large part of the south coast.

2.2 Sources of elevation data

2.2.1 Optical stereo imagery: SPOT5 & Pléiades

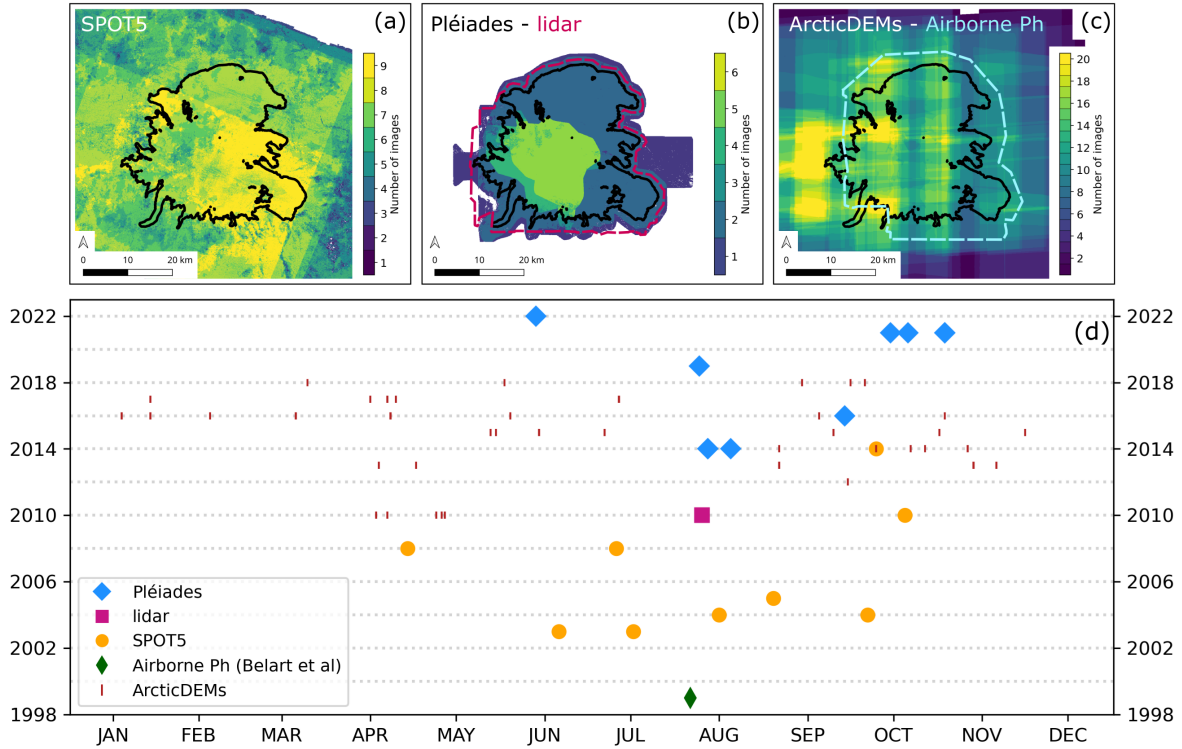


Fig. 2: Spatial extent of the studied scenes presented as the number of observations per pixel or as the outline of the scene. (a), (b) and (c) correspond to the number of SPOT5 DEMs, Pléiades DEMs and ArcticDEMs, respectively. The extent of the lidar DEM is indicated in dashed line on (b) and one of the Airborne photograph from Belart et al. (2020) is shown in dashed line on (c). The temporal distribution of all datasets is presented on (d).

Elevation data and stereo images. Optical stereo imagery products are commonly used to generate DEMs. Stereo images refer to a pair of images of the same location but taken from different angles. To do so, in-track stereo sensors acquire a first image (forward), continue a short time along the orbit and then acquire a second image (backward) either after rotating the sensor or by having two sensors with different look angles. Combined with information on the satellite position and orientation during the acquisition, elevation data can be derived (Fig. 3a) (Shean et al., 2016).

SPOT5-HRS. The 13 SPOT5 scenes used in this study come from the SPOT5 archive, a commercial Earth-imaging project from the French Space Agency (CNES). The dataset has recently been publicly opened thanks to the CNES Spot World Heritage Programme (<https://regards.cnes.fr/user/swh/modules/60>). It covered a time period from May 2002 to March 2015 and had a repeat cycle of 26 days. Stereo pairs were acquired thanks to the High-Resolution Stereoscopic (HRS) instrument which recorded forward and backward images with an angle of 20° ahead and behind the vertical respectively. The panchromatic band had a resolution of $10\text{ m} \times 5\text{ m}$ and the swath of the HRS was 120 km wide and 600 km long at maximum. SPOT5 HRS images from 2007 and after were acquired as part of the SPIRIT (SPOT 5 stereoscopic survey of Polar Ice: Reference Images and Topographies) project in 2007–2009 (Korona et al., 2009). Aiming to improve topography datasets of polar regions, a detailed archive of DEMs of polar ice masses, including the Icelandic ice caps, was generated.

Pléiades. Pléiades satellites have been in orbit since 2011. A total of eight stereo images were collected on request as part of the Dinamis CNES program (<https://dinamis.data-terra.org/>). The

satellites are on the same orbit as SPOT5. The swath of the sensor is 20 km large and Pléiades stereo images have a resolution of 0.5 m x 0.5 m. The potential of sub-meter stereo images for glacier mapping is now confirmed. Pléiades stereo images are highly precise (± 1 m) and offer valuable data to monitor glacier changes, as demonstrated in Berthier et al. (2014). Pléiades imagery thus constitutes an effective intermediate between coarse spaceborne images and high resolution airborne data.

2.2.2 Airborne lidar pointclouds

The Icelandic Meteorological Office, in collaboration with multiple institutes, has organised several airborne lidar (LIght Detection And Ranging) campaigns to map in detail all glaciers of Iceland (Jóhannesson et al., 2013). Mýrdalsjökull was surveyed in August 2010 and 2011 with a laser scanner operated 2500 m above the ground by the german company TopScan GmbH. Based on light transmission, the lidar technique enables to get very precise distances measurements. Light pulses emitted from the airborne system are reflected on the surface and recorded. Combined with simultaneous position and orientation data acquisitions from an integrated GPS, a 3D pointcloud is generated (Fig. 3b). The average density of measurements is ~ 0.33 pt.m⁻² (Jóhannesson et al., 2011) thanks to a 1200 m space between flight-lines and a swath width of 1800 m. Overcoming the limitations caused by surface texture or external light sources for traditional photographic methods, the airborne lidar allows to get measurements even when contrast is lacking, such as over accumulation areas. High resolution DEMs can then be derived from the obtained pointclouds. According to Jóhannesson et al. (2011), the expected accuracy is better than 0.5 m.

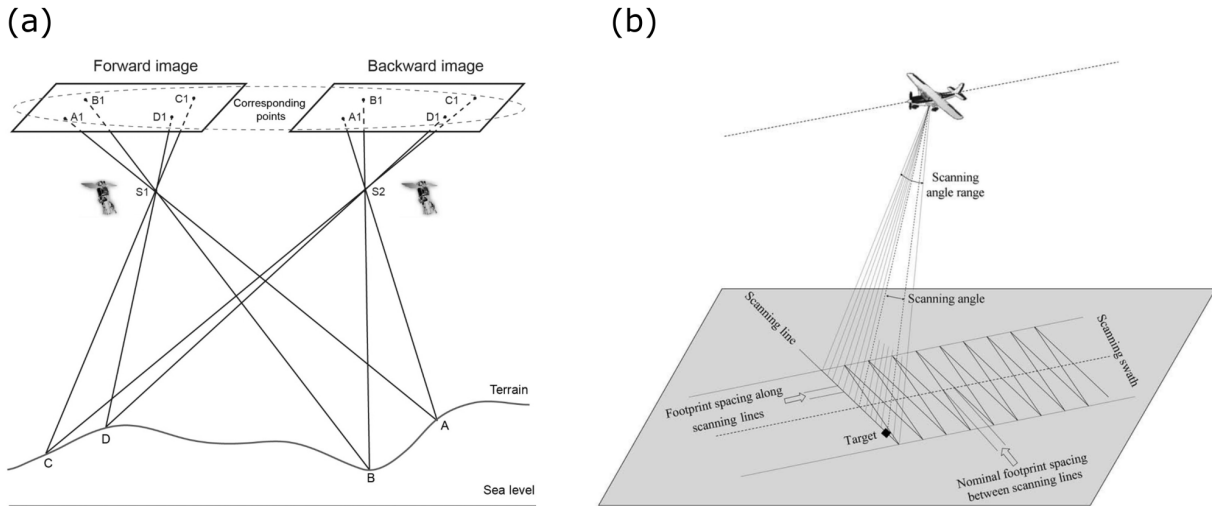


Fig. 3: (a) Principle diagram of DEM generation from stereo imagery (Wang et al., 2019). (b) Illustration of scanning attributes of lidar data acquisition (Gatziolis, 2008).

2.2.3 ArcticDEM dataset

The ArcticDEM database was produced by NGA–NSF (National Geospatial Intelligent Agency and National Science Foundation - USA) from the stereo satellites WorldView 1, 2 and GeoEye 1 (Porter et al., 2018). It covers all territories north of 60°N, including Iceland, and extends from 2015 to 2019. 90 DEMs in 2 m x 2 m resolution covering Mýrdalsjökull ice cap were extracted from this database and used in this study.

2.2.4 Aerial photogrammetry

A serie of photographs of Mýrdalsjökull from 1999 provided by the company Loftmyndir were processed in Belart et al. (2020) to produce a DEM following the processing guidelines described in Belart et al. (2019).

2.2.5 ASTER–ArcticDEM elevation change maps

Following Hugonnet et al. (2021) work, elevation change maps based on ASTER and ArcticDEM datasets are publicly available (<https://doi.org/10.6096/13>). To compare with the results of this study, maps of elevation difference of Mýrdalsjökull area on 5-year periods starting in 2000 were selected and analysed.

2.3 Outlines and ELA

Delineation of glacier and catchment outlines is an essential step in DEM analysis in order to differentiate glacierized areas from stable bareground terrain. Outlines of Mýrdalsjökull in 1999, 2003, 2010 and 2019 were used in this study. The 1999 outline was extracted from Belart et al. (2020) and the 2019 outline from Hannesdóttir et al. (2020). The 2003 and the 2010 outlines were manually delineated on the SPOT5 orthoimage from 2003-06-20 and on a shaded relief derived from the 2010-08-09 lidar DEM, respectively. To investigate changes at a local scale, three glacierized catchments were delineated: a northern divide, a southern divide and Kötlujökull divide using the same delineation criteria as Magnússon et al. (2021). The four glacier outlines and the extents of the glacierized catchments are shown in Fig. 1b. The Equilibrium Line Altitude (ELA), defined as the elevation of the separation line between the ablation area and the accumulation area, comes from Belart et al. (2020). It was obtained using the snowline at the end of the summer season as a proxy, based on a SPOT5 orthoimage from October 5th 2004.

2.4 Climatic data

Daily gridded temperature and precipitation data covering the period 1999–2019 were used in this study. The temperature dataset was extracted from Crochet and Jóhannesson (2011). Daily air temperature at 2 m above ground was obtained by interpolating observations from meteorological stations. The resulting gridded dataset has a resolution of 1 x 1 km. The precipitation dataset comes from the HARMONIE numerical model (Bengtsson et al., 2017; Nawri et al., 2017). Daily precipitation was computed at a 2.5 × 2.5 km resolution.

3 Methods

3.1 Creating elevation difference maps

3.1.1 DEM generation

First, DEMs were created from the raw satellite stereo images (SPOT5, Pléiades) and from the lidar pointclouds, using the Ames StereoPipeline (ASP) software (Shean et al., 2016). The lidar pointclouds were interpolated using ASP’s routine `point2dem`, into 2 x 2 m DEMs. The lidar DEMs from 2010 and 2011 were then mosaicked into a single DEM using the routine `dem_mosaic`.

The Pléiades stereo images were processed using the routines `mapproject`, `parallel_stereo` and `point2dem`, as described in Deschamps-Berger (2021). The SPOT5 stereo images were processed in a similar manner as the Pléiades images, with the addition of the pre-processing routine `add_spot_rpc`.

The temporal distribution of the DEMs collection is presented in Fig. 2 as well as the spatial extent of the original DEMs. It appears that most images were acquired either in June–July or September–October, which corresponds to the start and end of the summer period, respectively.

3.1.2 DEM co-registration

Prior to volume and mass calculations, potential biases in the DEMs have to be corrected. Using the DEMs without any correction could indeed lead to inaccurate estimates of glacier changes. These biases can be horizontal, vertical, planar tilt, or non-linear (e.g. jittering) (Girod et al., 2017; Hugonnet et al., 2022; Dehecq et al., 2020). Therefore, the first step in processing DEMs obtained from stereo imagery treatment consists of co-registering each DEM to a common reference DEM.

Nuth and Kääb algorithm. A robust co-registration method based on elevation difference and slope and aspect on stable terrain surrounding the glacierized area is proposed in Nuth and Kääb (2011). To consider only bareground terrain as a common stable area, glaciers are first masked out from the DEM using the Randolph Glacier Inventory (Consortium, 2017) glacier outlines. Then, the elevation difference dh between the two DEMs as well as the slope α and the aspect Ψ of the reference DEM are computed. To correct the secondary DEM to the reference one, the amplitude a and direction b of the shift vector between them and the overall elevation bias \overline{dh} have to be solved. Those parameters are related to slope, aspect and elevation difference as follow:

$$dh = a \cdot \cos(b - \Psi) \cdot \tan(\alpha) + \overline{dh}$$

A least square minimization is applied to solve the equation and obtain the three parameters. Several iterations of the process may be needed to get satisfying results as an analytical equation is solved using non-analytical variables (terrain is a non-analytical surface). Between two iterations, if the standard deviation on stable terrain is less than 2% or the amplitude of the shift vector a is less than 0.5 m, the iterating process is stopped.

Demcoreg tools. An automated and iterative implementation of this algorithm is available on the github repository *demcoreg* by David Shean (Shean et al., 2016) (<https://doi.org/10.5281/zenodo.5733-347>). A reference DEM and a secondary DEM to be corrected have to be provided. The IslandsDEM, a seamless and bias-corrected mosaic from ArcticDEM (Porter et al., 2018) and lidar (Johannesson et al., 2013) from the National Land Survey of Iceland (atlas.lmi.is/dem) was used as the reference DEM as it offers a complete coverage of a large area on and around the glacier. The co-registration was applied to all DEMs derived from Pléiades, SPOT5 and ArcticDEM. An example of the results from the co-registration process implemented in *demcoreg* are presented in Fig. 4.

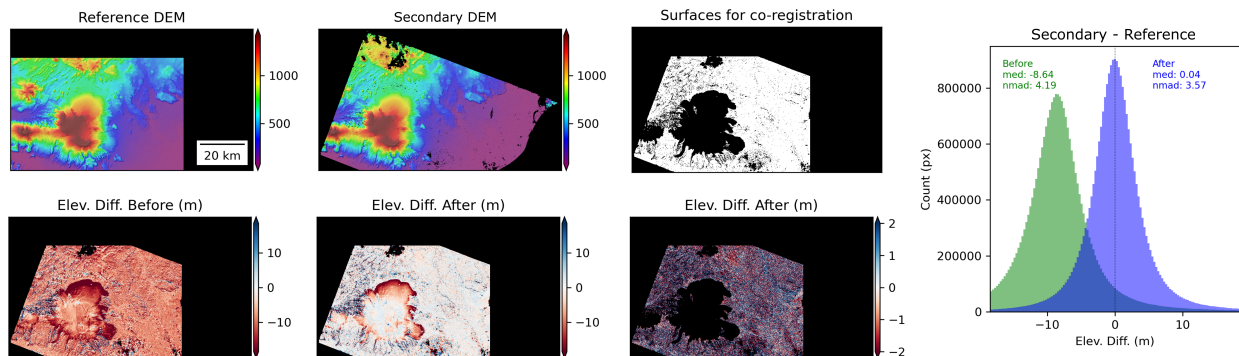


Fig. 4: Co-registration results from *demcoreg* tools applied to the 2014-10-09 SPOT5 DEM. After 11 iterations, the following corrections were obtained: x shift +3.36 m, y shift -22.62 m and z shift +8.64 m.

3.1.3 Filtering

According to the imagery and sensor characteristics, various artefacts can appear on the generated DEMs. The aberrant values can be caused by clouds, saturation in snow or dark areas, or errors at specific scan lines in the case of the SPOT5 data. An example of artefacts can be seen on the 2003-06-20 SPOT5 DEM (Fig. 5a), in the central and Southeast parts of the glacier. A filtering step is therefore required to remove incoherent elevation values that could affect further calculations. For this purpose, different types of filters can be used, either based on the computed elevation maps or on the initial DEMs. Two filtering methods were here applied, compared and eventually combined to improve the performance. This combination was then used on all the DEMs generated from SPOT5 and ArcticDEM datasets as well as on the 1999 DEM from aerial photographs.

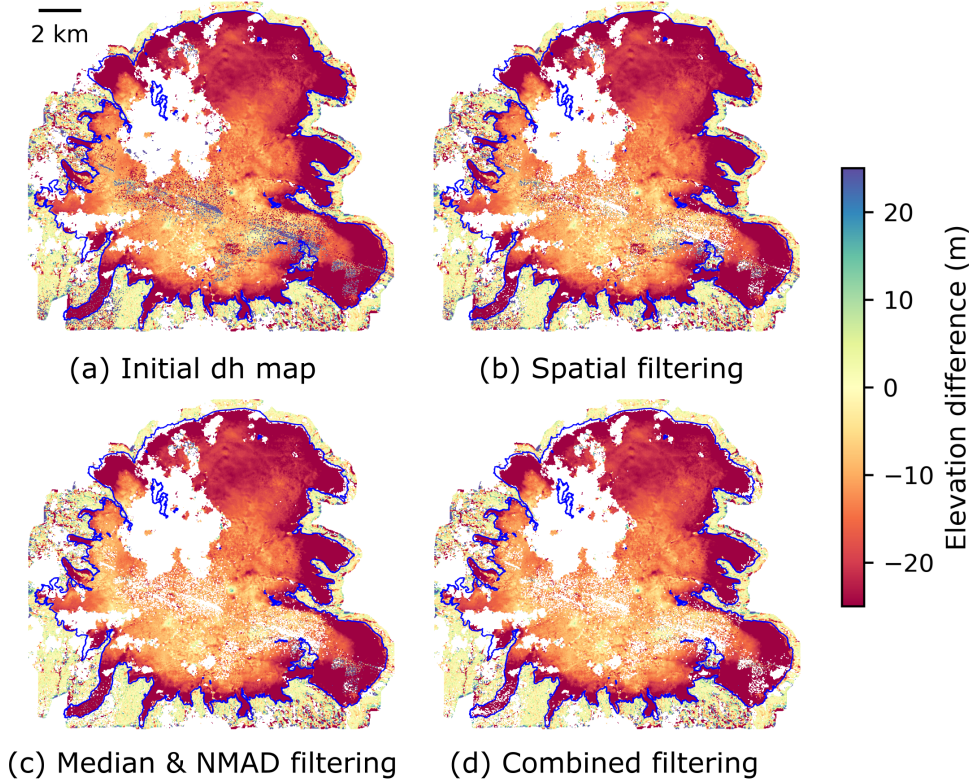


Fig. 5: Comparison of filtering methods applied to the 2003-06-20 SPOT5 DEM. The corresponding dh maps with the 2010-08-09 Lidar DEM are presented for better visualisation. (a) Initial dh map. (b) Spatial filtering with a radius of 50 m and a threshold of 50 m. (c) Median & NMAD filtering with a threshold of 10. (d) Combination of both filtering methods. The 2003 outline is shown in blue.

Spatial filtering. Following Hugonnet et al. (2021), a spatial filter based on a comparison between the DEM to be filtered and a reference DEM was applied. The mosaicked lidar DEM was used as the reference DEM. For each pixel, the maximum max_{pix} and minimum min_{pix} elevation of the reference DEM within a r radius area were calculated. Then, all pixels where the elevation is larger than $max_{pix} + dh_{thresh}$ or smaller than $min_{pix} - dh_{thresh}$ were masked, with dh_{thresh} corresponding to the elevation threshold. After several tests, the radius r was set to 10 m and the dh_{thresh} to 50 m. Fig. 5b illustrates the spatial filtering method for the 2003-06-20 SPOT5 DEM. The majority of the artefacts are removed, but some aberrant values still remain in the East and Southwest parts.

Median & NMAD filtering. Another filtering approach consists of using statistical characteristics of a DEM dataset to identify incoherent values. The normalized median absolute deviation (NMAD) is a metric to evaluate the data dispersion. It is less sensitive to outliers than the standard deviation and thus widely used to estimate DEMs vertical precision (Höhle and Höhle, 2009). NMAD is computed as follow:

$$NMAD = 1.4826 \cdot median(|\Delta h_j - m_{\Delta h}|)$$

where Δh_j is the individual error and $m_{\Delta h}$ the median of the errors. Considering all DEMs used in this study (i.e. 1999 airborne DEM, SPOT5, Pléiades, lidar and ArcticDEM), a median mosaic and a NMAD mosaic were computed. In other words, for each 10 m x 10 m pixel of the mosaic, a median and NMAD value of all the possible elevations available were calculated. Then, a threshold K was set so that for each DEM analysed, a pixel would be considered an outlier if its elevation was larger than its $median \pm (K * NMAD)$. Following several tests, the threshold was adjusted to 10 m for all DEMs. The result of this filtering method on the 2003-06-20 SPOT5 DEM is shown in Fig. 5c. As for spatial filtering, aberrant values also remain in the East and Southwest parts.

Combination. To remove the artefacts observed on DEMs, a combination of the spatial filter and the median NMAD filter proved to be the most efficient method. Taken separately, both filtering methods would keep incoherent elevations at different places. Thus, the majority of the aberrant values were removed using the combined filtering (Fig. 5d).

3.1.4 Elevation difference computation

Before starting the elevation difference computation between pairs of DEMs, a pairwise co-registration had to be computed. Even though the DEMs were all co-registered to a reference DEM, some residuals could still remain and potentially be noticeable in further calculations. For each DEM pair, the oldest DEM was considered as the reference DEM. The amplitude of the horizontal and vertical shifts of this pairwise co-registration was systematically less than 1 m, i.e. one order of magnitude lower than the first co-registration. Then, the elevation difference between the most recent DEM and the oldest DEM of the pair was computed. To get consistent and comparable elevation difference maps (*dh* maps), DEMs were resampled to a 10 m x 10 m pixel size. Fig. 6 is an example of the *dh* maps obtained.

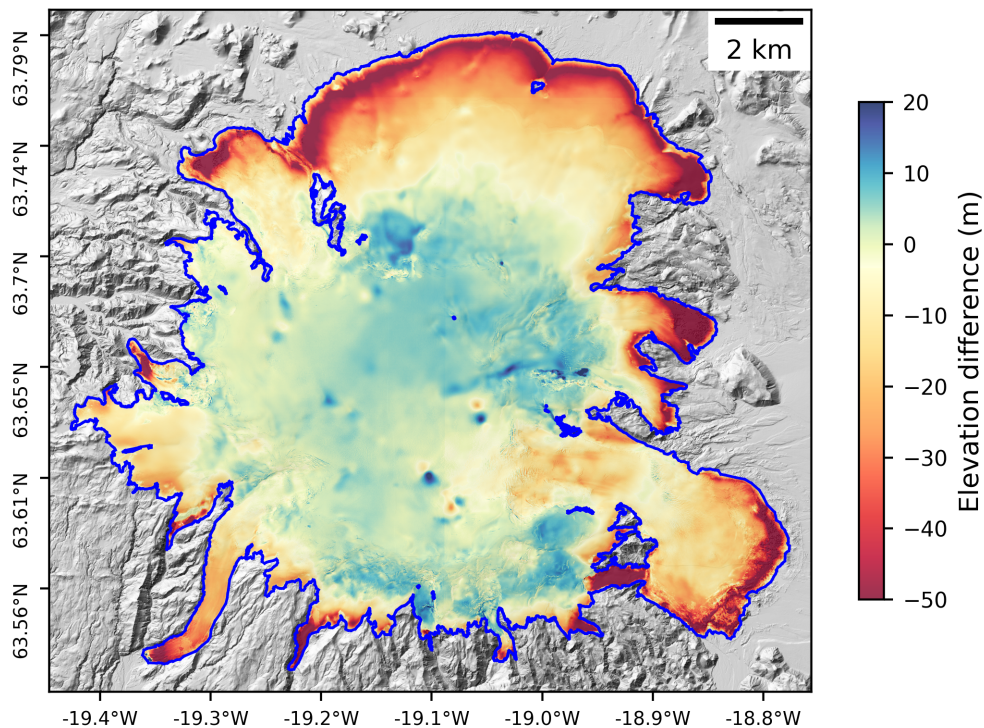


Fig. 6: Elevation difference map between 2010-08-09 Lidar DEM and 2021-11-02 Pléiades DEM (both interpolated).

3.1.5 Interpolation

Most of the DEMs used in this study contain data gaps, mainly due to clouds, filtering or partial coverage of the initial stereo images (Fig. 7a). The amount of lacking data also depends on the nature of the sensor. For example, SPOT5 DEMs, often noisy, show much more voids than Pléiades or lidar DEMs. Since complete *dh* maps are required to calculate volume and mass changes, an interpolation step is therefore necessary. A variety of void interpolation methods are available (McNabb et al., 2019), either on original DEMs or on *dh* maps. Spatial methods fill gaps by linearly interpolating values around voids whereas hypsometric methods use an assumed relationship between elevation and elevation change to interpolate data gaps. However, the selection of a method can directly impact volume and mass estimates. Two methods were identified in McNabb et al. (2019) as best-performing and leading to reliable estimates: the spatial interpolation and the local mean hypsometric interpolation. They were first applied separately to perform a comparison of their efficiency. Then, a combination of both

methods starting with the spatial interpolation appeared to be an appropriate approach for the studied datasets.

Spatial interpolation of dh maps. Starting with the original dh map of two unfilled DEMs, resulting voids are filled using a bilinear interpolation (McNabb et al., 2019). This method performs very well on small gaps as elevation changes on glaciers generally present a similar trend on reduced areas (Fig. 7b). However, it becomes less adequate when elevation difference maps exhibit very large gaps (>200 pixels). Far away from voids borders, the spatial interpolation poorly accounts for potential local variations in elevation change. Interpolation artefacts also induce larger uncertainties as gaps get larger.

Local mean hypsometric interpolation of dh maps. This method is also applied to the initial dh map of two unfilled DEMs. First, the elevations are grouped into 50 m-bins according to the elevation of a complete reference DEM. Then, the relationship between elevation and elevation difference is obtained by calculating for each bin the mean elevation difference. Voids are eventually filled using the elevation from the reference DEM and the corresponding value from the computed relationship (McNabb et al., 2019). This approach is effective on both small and large data gaps. However, it tends to smooth the original elevation change patterns and often produces discontinuities at voids borders. Those effects are clearly visible on Fig. 7c.

Combination. Considering the pros and cons of each method, we decided to compute a combined interpolation as follows. First, a spatial interpolation was applied in order to preserve gradual and continuous changes as much as possible around gaps. Then, a local hypsometric interpolation was used to fill the larger remaining voids. The complete elevation maps thus obtained were used in further calculations (Fig. 7d).

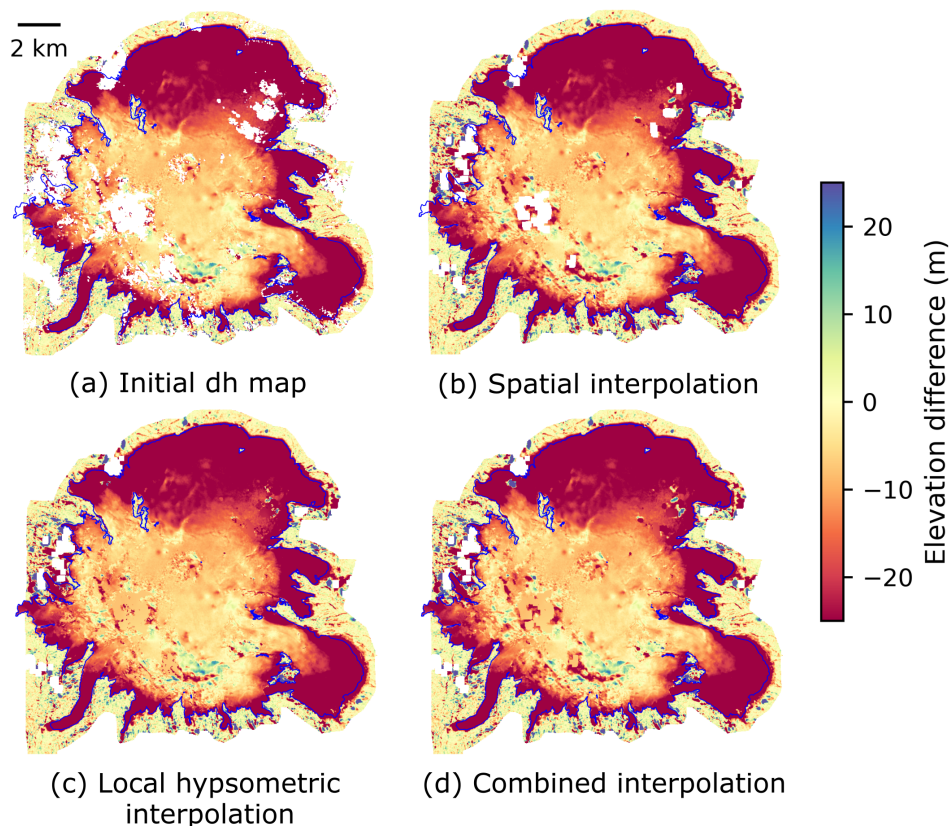


Fig. 7: Comparison of interpolation methods applied to the dh map between 2004-10-05 SPOT5 DEM and 2010-10-19 SPOT5 DEM. (a) Initial dh map. (b) Spatial interpolation. (c) Local hypsometric interpolation. (d) Combination of both methods. The 2019 outline is shown in blue.

3.1.6 Gaussian Process regression

In order to compute volume changes and mass balance, a preliminary approach consists of using elevation difference maps created from the fixed-date DEMs previously pre-processed. However, this method presents some limitations. In particular, two DEMs acquired on dates more than one month apart require a correction for their dh map to show elevation and volume changes without being affected by seasonal signals. DEMs can be seasonally corrected individually using snow accumulation and melting models adjusted with climatic records as in Belart et al. (2019, 2020). Still, this process is time-consuming and complicated to use when a large number of DEMs is considered. Consequently, alternative numerical methods have been developed to overcome those issues and to obtain continuous synthetic datasets out of scattered observations. Considering all DEMs as a stack, a temporal regression can be computed for each pixel to produce a gapless time series of elevation maps. Then, volume and mass balance estimates can be calculated on precise time windows, which is significantly more accurate for glaciological analysis.

The straightforward and most common method is to apply a linear regression (possibly weighted with the uncertainties) solved with least squares (Berthier et al., 2016; Brun et al., 2017). Nevertheless, this approach has multiple drawbacks. On one hand, this type of regression can depict a long-term tendency (Dussailant et al., 2019) but does not take into account seasonal or annual trends. On the other hand, non-linear variations, quite common in glacier dynamics (surges, accelerated thinning events), are not accounted for.

Hugonnet et al. (2021) introduced the use of a state-of-the-art regression method in DEM processing, the Gaussian Process regression (GP). This approach, developed by Williams and Rasmussen (2006), is part of the generic supervised learning methods and constitutes an alternative to the classic linear regression. In addition to accounting for non-linear changes, it also has the advantage of being non-parametric. In other words, this method does not require to define in advance the number of parameters or to have a precise idea of the function to be fitted to the observations. Instead, it adjusts the statistical characteristics to match the observed data.

The whole statistical process is based on the following assumption: considering the function that describes the data, the values that it takes are presumed to be random variables that follow a normal distribution. To rephrase this, it is assumed that the set of observations comply with a multivariate normal distribution. Then, the aim of the GP is to find the mean vector and the covariance matrix that characterize this multivariate normal distribution. To accomplish this, the method defines a kernel function, assumed to model the covariance matrix, which is used to guide the regression. It is important to note that the choice of a kernel, i.e. the model of variance, is essential. For the GP to correctly reproduce the multivariate normal distribution, it is capital to find a kernel function that accurately models the similarities between data points distributed in time or space. According to the dataset specificities, different kernels can be chosen and possibly combined. Then, the selected kernel is adjusted to the dataset to obtain the regression model and estimates can eventually be done where observations are missing.

The GP adapted to DEM processing is implemented in the github repository *pyddem* (<https://pypi.org/project/pyddem/>) by Hugonnet et al. (2021). The selected combination of kernels accounts for: a long-term trend (PL, pairwise linear kernel), a seasonal trend (ESS, periodic exponential sine-squared kernel), the proximity of elevation changes with varying time differences (RBF, local radial basis function kernel), non-linear trends (RQ, rational quadratic kernel multiplied by a linear kernel) and the average of measurement errors at time t (white noise $\sigma_{wn}(t, x, y)$).

$$\sigma_h(x, y, \Delta t)^2 = PL + ESS + RBF + RQ * PL + \sigma_{wn}(t, x, y)^2$$

The Gaussian Processing Regression was run using a stack of 134 DEMs co-registered to the IslandsDEM composed of 116 ArcticDEM, 9 SPOT5 DEMs, 8 Pléiades DEMs and 1 Airborne photogrammetry DEM. The lidar DEM was intentionally not included in the stack for later validation of the GP results. Because of computing limitations, GP was run at a maximum spatial resolution of 15 m x 15 m and a 30-day time step during the period 1999–2021. As a result, a dataset of 264 synthetic DEMs was obtained. Examples of the elevation difference maps based on the synthetic, spatially and temporally homogenized DEMs generated with the GP method are shown in Fig. 8.

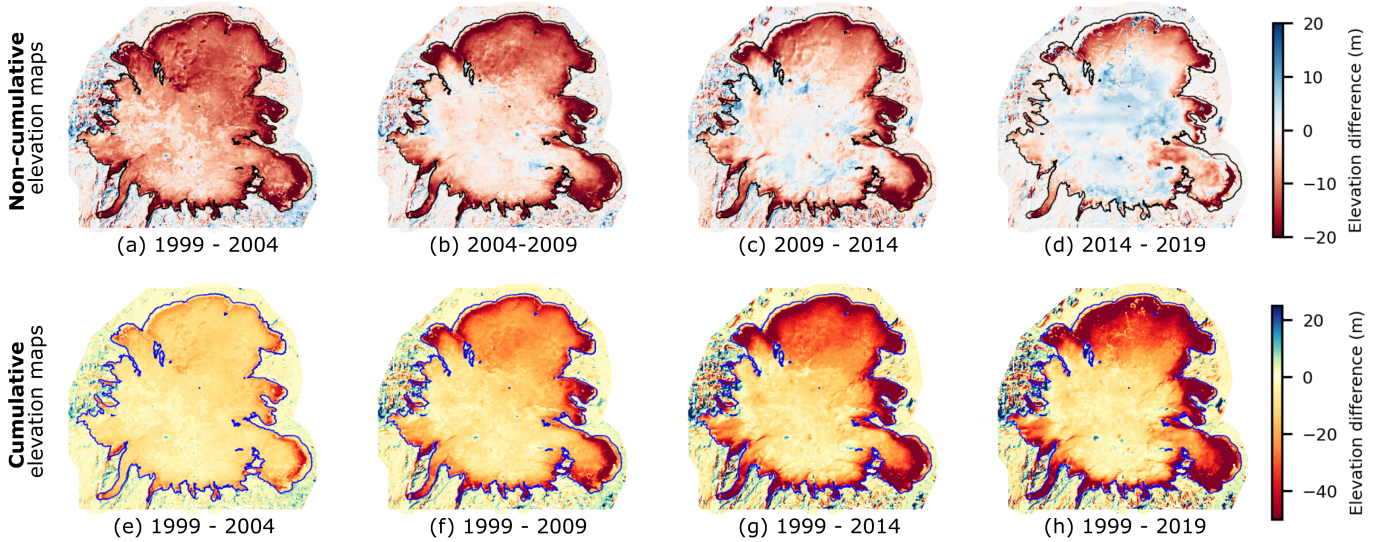


Fig. 8: Non-cumulative (upper panels) and cumulative (lower panels) elevation difference maps computed with synthetic GP-generated DEMs. Elevation difference was calculated on periods of 5 hydrological years (October 1st to September 30th) starting in 1999. The 1999 outline is shown in blue and black.

3.2 Mass balance computation

3.2.1 Volume change and mass balance

In order to investigate glacier changes over time, several indicators can be computed. First, using complete dh maps, the total volume change during the corresponding period was calculated as $\Delta V = \overline{\Delta h} \cdot A_{ini}$, where $\overline{\Delta h}$ (m) is the mean elevation change and A_{ini} (m²) the area of the glacier at the earliest date. For the years 1999, 2003, 2010 and 2019, the area was directly extracted from the outline shapefiles. Otherwise, a linear interpolation of the area was computed for intermediate years based on those four values. To be consistent with glaciological conventions, hydrological years, defined as October 1st to September 30th, were taken as a reference period in all further calculations.

Then, when the observation period Δt (years) exceeds 4 years, the geodetic mass balance rate \dot{B} (m w.e. a⁻¹) was obtained as follow:

$$\dot{B} = \frac{\Delta V \cdot f_{\Delta V}}{\bar{A} \cdot \Delta t}$$

where $f_{\Delta V}$ (kg·m⁻³) is the conversion factor from volume to mass change and $\bar{A} = \frac{1}{2} \cdot (A_{ini} + A_{end})$ is the average area on the observation period. Following Huss (2013), $f_{\Delta V}$ was set to 850 ± 60 kg·m⁻³. However, it is crucial to note that this value cannot be used with high confidence on shorter periods (<4 years) (Huss, 2013). As the density of melted and accumulated snow can significantly change from one year to the next, applying this constant value of the conversion factor to transform volume into mass change can lead to an over or under estimation of mass changes. The values obtained over periods of one to three years can thus only give a coarse estimate of the mass balance.

In order to study the local variability of mass balance, three subregions of the ice cap were defined, separated by the ice divides described in the data section. As the northern and southern outlets are exposed to different climatic regimes, two corresponding areas were delineated: Sléttjökull and Öldufellsjökull outlets were included in the northern catchment, Goðalandsjökull and Sólheimajökull outlets were encompassed in the southern one. Kötlujökull was defined as a separate area. Catchments outlines can be found on Fig. 1b and are reminded on Fig. 12. Mass balance was calculated on the three glacierized catchments using the same methodology as for the complete ice cap, i.e. using the same maps of elevation difference, except they were cropped to the three respective subregions. Values shown in Fig. 12 were obtained with the GP-generated synthetic DEMs. Mass balance was calculated on periods of one and four hydrological years between 1999 and 2020. For simplicity, the uncertainties

calculated on the stable terrain around Mýrdalsjökull were used for the catchments mass balance estimates.

3.2.2 Uncertainties

To get an order of magnitude of the uncertainty in mean elevation difference, the NMAD on stable terrain can be used as a first estimate (e.g. Höhle and Höhle (2009)). However, this approach does not take into account non-stationarities and spatial correlations. As a result, this initial calculation tends to largely overestimate the uncertainty. Therefore, we preferably used the method developed by Hugonnet et al. (2022) to determine the uncertainty in mean elevation difference $\sigma_{\overline{\Delta h}}$.

This approach takes into account two statistical effects that are often not considered in elevation error estimates. First, elevation maps present significant non-stationarities. To rephrase it, there is a precision variability in the elevation observations related to the terrain or instrument variables. To obtain an estimate of the elevation uncertainty, non-stationarities are numerically modelled using different explanatory variables (terrain slope and curvature). Second, elevation errors are spatially correlated (e.g. Rolstad et al. (2009); Magnússon et al. (2016)). In other words, the respective elevation errors of two close pixels cannot be considered as independent. This spatial correlation can be of multiple ranges: short-range (related to the DEM resolution) or long-range (linked to instrument noise and imperfections). Using variograms (Fig. 9) and pairwise sampling, spatial correlations are modelled and included in the elevation uncertainty computation. Tools to apply this method of elevation errors calculation are implemented in the github repository *xDEM* (<https://doi.org/10.5281/zenodo.4809698>).

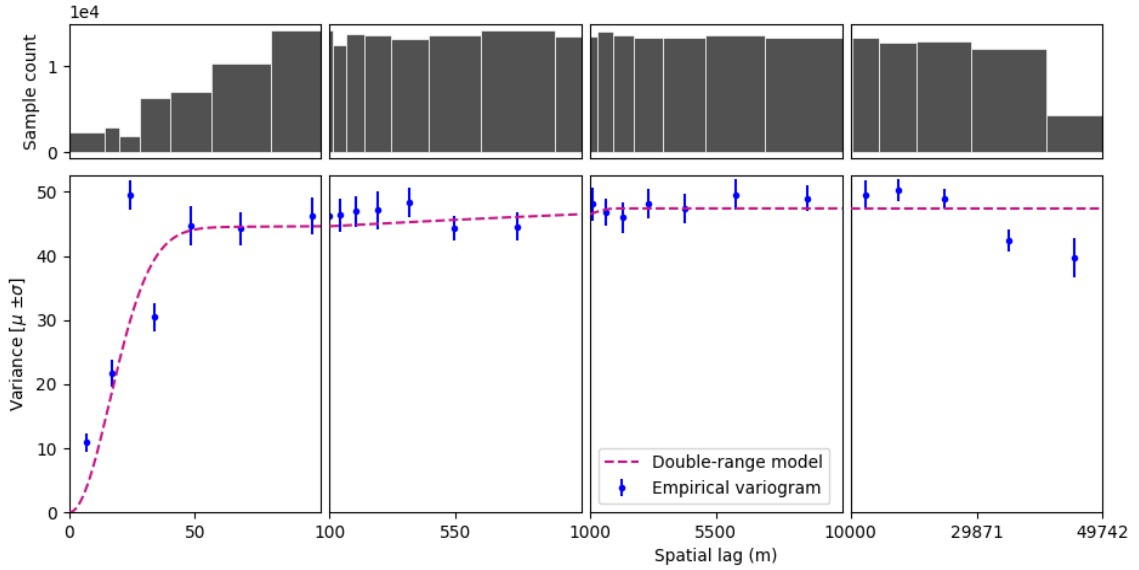


Fig. 9: Variogram obtained on stable terrain from the dh map between 2003-07-16 and 2008-07-09 SPOT5 DEMs using *xDEM* tools. A short-range correlation (until ~ 100 m) and a long-range correlation (from ~ 1000 m) can be identified. The double-range spherical function used to model the variogram accounts for both correlation ranges.

Then, assuming that the glacier area and the mean elevation difference are not correlated, the uncertainty in volume change was expressed as follow:

$$\sigma_{\Delta V}^2 = (\overline{\Delta h} \cdot \sigma_{\overline{A}})^2 + (\overline{A} \cdot \sigma_{\overline{\Delta h}})^2$$

Next, the uncertainty σ_m in the geodetic mass balance was computed, using the propagation of uncertainties formula:

$$\begin{aligned} \sigma_m^2 &= \left(\frac{\partial \dot{B}}{\partial \Delta V} \cdot \sigma_{\Delta V}\right)^2 + \left(\frac{\partial \dot{B}}{\partial f_{\Delta V}} \cdot \sigma_{f_{\Delta V}}\right)^2 + \left(\frac{\partial \dot{B}}{\partial \overline{A}} \cdot \sigma_{\overline{A}}\right)^2 \\ &= \left(\frac{f_{\Delta V}}{\overline{A} \cdot \Delta t} \cdot \sigma_{\Delta V}\right)^2 + \left(\frac{\Delta V}{\overline{A} \cdot \Delta t} \cdot \sigma_{f_{\Delta V}}\right)^2 + \left(-\frac{\Delta V \cdot f_{\Delta V}}{\overline{A}^2 \cdot \Delta t} \cdot \sigma_{\overline{A}}\right)^2 \end{aligned}$$

where $\sigma_{f_{\Delta V}} = 60 \text{ kg}\cdot\text{m}^{-3}$ is the conversion factor uncertainty and $\sigma_{\bar{A}}$ is the area uncertainty calculated as 5% for the average area \bar{A} . As for volume uncertainty, the variables were assumed to be independent.

3.3 Climate analysis

3.3.1 Temperature and precipitation data processing

Summer temperature. For the purpose of this study, temperature data was only selected at the ELA using a 100 m buffer around it. To extract the right data at this narrow zone, the temperature dataset was resampled using a cubic convolution to a 50 m x 50 m pixel size. Defining summer from May 21st to September 30th, the mean summer temperature was computed for each year from 1999 to 2019. The average summer temperature map of Mýrdalsjökull over the whole period is shown in Fig 1c.

Winter precipitation. As for the temperature dataset, a cubic resampling was applied to precipitation grids in order to extract data on the 100 m buffer around the ELA. For each year, winter precipitation was calculated as the sum of daily precipitation from January 1st to May 20th and from October 1st to December 31st from the previous year. Contours of the average winter precipitation per year on Mýrdalsjökull between 1999 and 2019 are presented in Fig 1c. For further analysis, precipitation was normalized and was divided by the average winter value on the glacier between 1999 and 2019 (5.453 m).

3.3.2 Linear model of climate forcing

As described in Belart et al. (2019), a preliminary way to investigate the relationship between climate and glacier changes is to compute a linear regression connecting mass balance values and climatic variables, specifically summer temperature and winter precipitation, which are the main forcing parameters to glacier mass balance. Correlating the mass balance to the climatic records enables estimating mass balance sensitivities that quantify the glacier response to climate variability. However, the conventional (i.e. geodetic or glaciological) mass balance is affected not only by climate variations but also by the dynamic adjustments of the glacier (size, geometry) (Engelhardt et al., 2015). Therefore, using the reference-surface mass balance, defined as the equivalent mass balance over a fixed geometry, enables to isolate the relationship between glacier mass balance and climate variations. A correction has then to be applied to relate reference-surface and conventional mass balance. Assuming that the mass balance can be expressed as a linear combination of climatic variables, the following equation can be written:

$$\dot{B} = \phi T_s + \omega P_w + \gamma \Delta A + k \quad (1)$$

where \dot{B} is the geodetic mass balance over a certain time window, T_s is the mean summer temperature, P_w the mean winter precipitation and ΔA the area difference between the 1999 reference and the average area during the time window. T_s and P_w were calculated at the equilibrium line altitude (ELA), which is assumed to be reasonably constant during the study period.

The parameters ϕ and ω correspond to the mass balance sensitivity to a 1°C warming in summer temperature ($\frac{\partial \dot{B}}{\partial T_s}$) and a 10% increase in winter precipitation ($\frac{\partial \dot{B}}{\partial P_w}$) respectively. The parameter γ , associated with the reference surface term ΔA , introduces the adjustment between conventional and reference-surface mass balance. It also significantly improves correlation results (Cogley, 2011; Huss and Farinotti, 2012). Eventually, the offset correction parameter k encompasses both non-linear effects and contributions of other variables not considered in the simplified model.

Parameters were found using a least-squares fit of Eq. (1) weighted with mass balance uncertainties. To get meaningful mass balance values, non overlapping four-year time periods from 1999 to 2019 were considered. Finally, the annual synthetic mass balance was calculated using the obtained parameters in Eq. (1) with annual summer temperature, winter precipitation and glacier area data. The linear model was applied to the whole ice cap and to the three glacierized catchments.

4 Results

4.1 Elevation time series

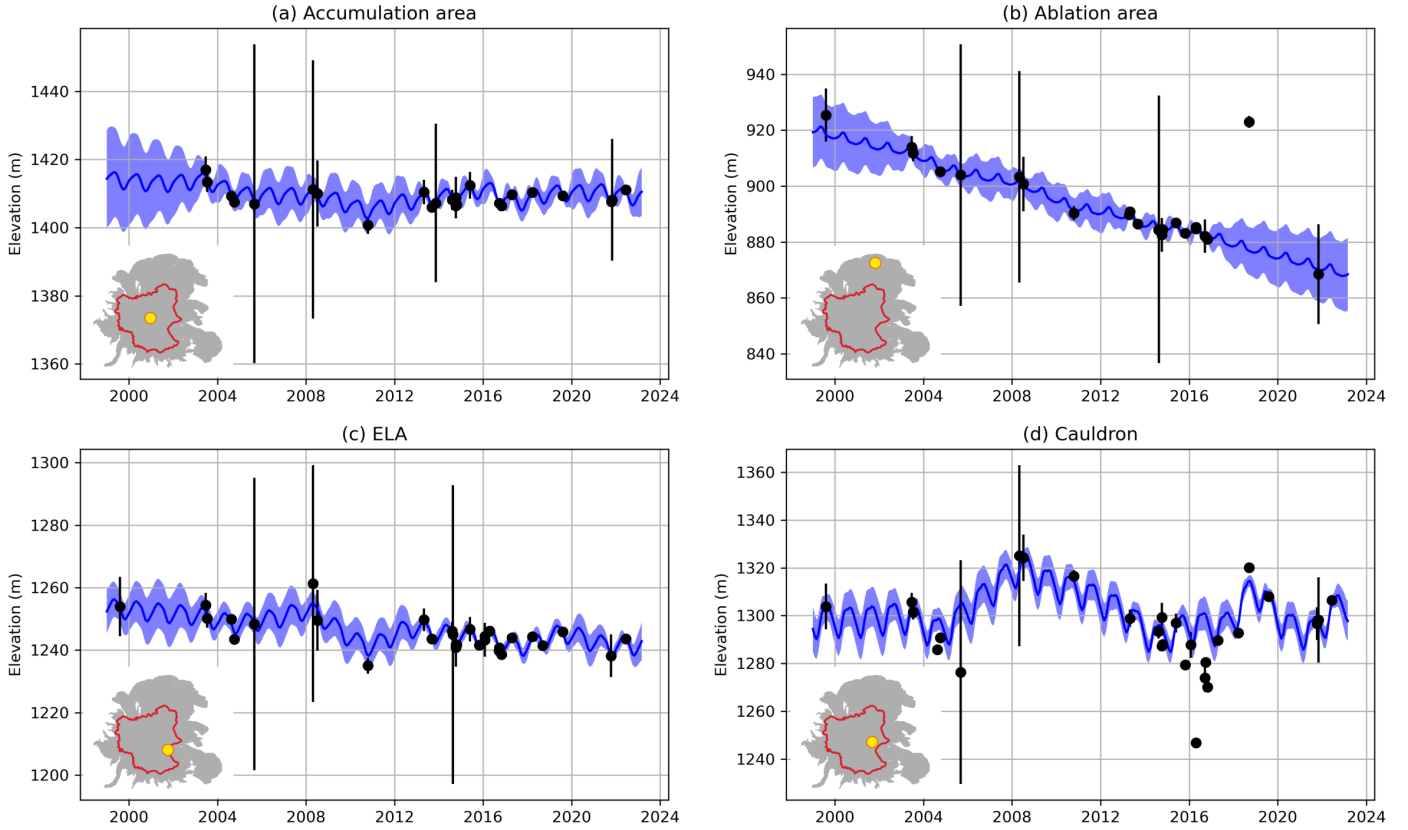


Fig. 10: Elevation time series obtained from GP regression for pixels from different locations on Mýrdalsjökull: **(a)** Accumulation area, **(b)** Ablation area, **(c)** ELA, **(d)** Cauldron. The blue line corresponds to the GP regression time series. The associated 1σ interval is indicated in blue. The original elevations and their uncertainty are shown as black dots and vertical lines.

As the result of the GP regression, a time series of elevation with a time step of 30 days was generated for each 15×15 m pixel of Mýrdalsjökull. In order to illustrate the variety of patterns that are encompassed by the GP regression, four pixels from diverse locations were selected: from the accumulation area, from the ablation area, from the ELA and from a cauldron. The corresponding elevation time series are presented in Fig. 10, as well as the 1σ interval and the original elevation data. The elevation trends in the period 1999–2019 are very contrasted according to the location. Differences in the amplitude of the seasonal signal are also noticeable. The elevation time series from the accumulation area is steady over the two decades, slightly decreasing from 1999 to 2012 and then gently increasing until 2016 before levelling off. The seasonal variation, around ~ 5 m, is rather large. On the ablation area, the expected elevation decrease is remarkably clear, almost reaching -50 m in 20 years with an attenuated seasonal signal. In contrast, the pixel at the ELA does not show such a clear trend. The elevation is broadly declining over the study period but contains short periods of rising elevation (2005–2008, 2011–2013). Last, the elevation time series at the cauldron is erratic: periods of elevation increase and decrease alternate with no clearly identified frequency and the seasonal variation is substantial. Overall, the 1σ interval is larger when the original elevation data are scarce. For example, the elevation time series of the pixel from the accumulation area presents considerable uncertainties before 2004 as no data are available for the GP regression. On the other hand, the period 2013–2017, which contains a large number of observations, is much better constrained and leads to a reduced 1σ interval.

4.2 Geodetic mass balance

Before using GP-generated DEMs for mass balance computation, a validation comparison between the lidar DEM from 2010-08-09 and the closest synthetic DEM (2010-08-01) was performed. The dh map between the two DEMs was computed. The NMAD was then calculated on the glacier area (3.33 m) as a proxy of the precision. Using the co-registration tools without masking the glacier, a shift of +1.66 m (x), +6.74 m (y) and +0.58 (z) between the two DEMs was obtained. Following those results, comparable to SPOT5 DEMs precision and to the shifts obtained with the pairwise co-registration, further calculation were performed.

First, mass balance $\dot{B}_{dh\ map}$ were calculated using the original elevation difference maps. The latter were computed only on significant time periods, implying that a selection had to be made from all possible combinations of DEMs pairs. A total of eight DEM pairs were highlighted as they fulfilled the two following criteria: be acquired at least four years apart and at the same time of year (<1 month difference). The corresponding mass balance range between -0.27 ± 0.33 m w.e. a^{-1} (2010-10-19 to 2014-10-09) and -2.85 ± 0.14 m w.e. a^{-1} (2008-07-09 to 2010-08-09), with a large decrease in 2010 followed by less negative values during the past decade.

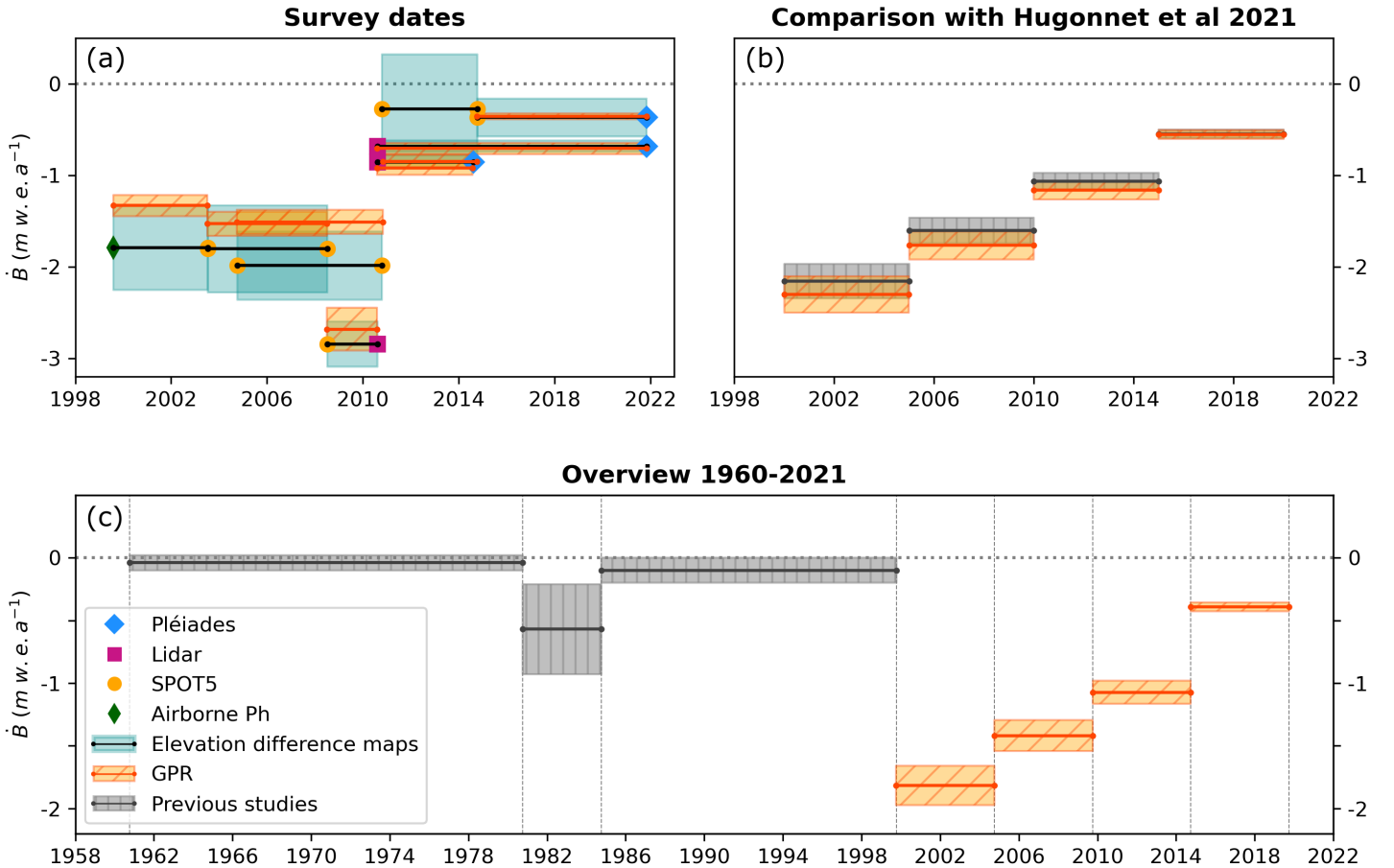


Fig. 11: Mass balance results. **(a)** Mass balance computed on survey dates (eight maps of elevation difference). Values and uncertainties obtained with the original elevation difference maps are shown in blue. Synthetic GP results are plotted in orange. **(b)** Comparison between mass balance obtained with the elevation change maps from Hugonnet et al. (2021) (grey) and synthetic GP results (orange). For consistency with Hugonnet's results, this comparison was done using the synthetic DEMs created from January 1st to December 31st. Periods of 5 years starting in 2000 are considered. **(c)** Mass balance overview from 1960 to 2021. Previous results from Belart et al. (2020) are shown in grey, GP mass balance on 5-hydrological-year periods are indicated in orange.

Secondly, the geodetic mass balance was also estimated using the synthetic GP-generated DEMs \dot{B}_{GP} . In order to validate the results obtained with the Gaussian Processing regression, a comparison

with the original elevation difference maps was performed. For each survey date, the temporally closest synthetic DEM was extracted to compute the synthetic elevation difference map equivalent to the original one. Mass balance using both maps were compared on the eight different periods (Fig. 11a).

Overall, both methods lead to similar mass balance. The \dot{B}_{GP} is systematically included in the uncertainty bar of the original dh map value $\dot{B}_{dh\ map}$. It is to be noted that when the elevation difference map includes at least one Pléiades or lidar DEM, the two estimates show a good agreement. For example, the $\dot{B}_{dh\ map}$ between 2008-07-09 SPOT5 DEM and 2010-08-09 lidar DEM is -2.85 ± 0.14 m w.e. a^{-1} , compared to the \dot{B}_{GP} of -2.68 ± 0.23 m w.e. a^{-1} computed between 2008-07-01 to 2010-08-01. However, when two SPOT5 DEMs or one SPOT5 DEM and the airborne photogrammetry DEM are involved, the agreement is worse. First, the $\dot{B}_{dh\ map}$ uncertainties are much larger than those of \dot{B}_{GP} . Then, \dot{B}_{GP} overlap only at the extremity of the uncertainty bar, with both less negative (August 1999 to July 2003, July 2003 to July 2008, October 2004 to October 2010) and more negative (October 2010 - October 2014) values than $\dot{B}_{dh\ map}$. Those observations could be explained by the higher level of noise of the SPOT5 and airborne photogrammetry DEMs.

Another comparison was performed with the mass balance \dot{B}_{Hug} computed with the elevation change maps from Hugonnet et al. (2021). These were obtained by applying the same GP method to ASTER and ArcticDEM DEMs datasets. As elevation data were only available on January 1st to December 31st years, we adapted the $\dot{B}_{GP_{Jan}}$ calculation to this period definition for consistency (see Fig. 11b). Mass balance from this study tend to be less negative than those obtained here. Nevertheless, error bars are overlapping for each period and the central values \dot{B}_{GP} and \dot{B}_{Hug} are always included in the error bar of the other respectively. Thus the two studies show a good agreement.

To get a longer perspective of mass balance over the past decades, estimates for the period 1960–1999 were extracted from Belart et al. (2020) (Fig. 11c, Table 1). Whereas \dot{B} is pretty stable and close to 0 m w.e. a^{-1} during the second half of the twentieth century, the annual mass balance drops in the early 2000s to -1.82 ± 0.16 m w.e. a^{-1} before becoming gradually less negative.

Period	\dot{B} (m w.e. a^{-1})
1960–1980	-0.04 ± 0.06
1980–1984	-0.57 ± 0.36
1984–1999	-0.10 ± 0.10
1999–2004	-1.82 ± 0.16
2004–2009	-1.42 ± 0.12
2009–2014	-1.07 ± 0.09
2014–2019	-0.39 ± 0.03

Table 1: Mass balance from 1960 to 2019

4.3 Catchment scale analysis

The observed general trend of mass balance is the same for the three glacierized catchments and for Mýrdalsjökull ice cap. On the two past decades, mass balance rates become slowly less negative and almost reach positive values over the period 2011–2015. Mass balance ranges from -2.07 ± 0.13 m w.e. a^{-1} (2003–2007) to -0.76 ± 0.06 m w.e. a^{-1} (2015–2019) for the northern catchment, from -1.39 ± 0.14 m w.e. a^{-1} (1999–2003) to -0.20 ± 0.04 m w.e. a^{-1} (2011–2015) for the southern catchment and from -1.49 ± 0.14 m w.e. a^{-1} (1999–2003) to -0.56 ± 0.04 m w.e. a^{-1} (2011–2015) for Kötlujökull. The second to last period, especially the years 2014 and 2015, is known for a rather cold and wet climate in Iceland (e.g. Aðalgeirsdóttir et al. (2020)), which would explain the near-zero mass balance observed for these catchments. However, this general trend might not to continue as suggested by the decrease of annual mass balance rates after 2017. Four-year mass balance rates for the three catchments and for entire Mýrdalsjökull are also indicated in Table 2.

In accordance with the elevation difference maps from Fig. 8, the northern catchment has the most negative mass balance and the southern catchment has the less negative ones. Kötlujökull behaves

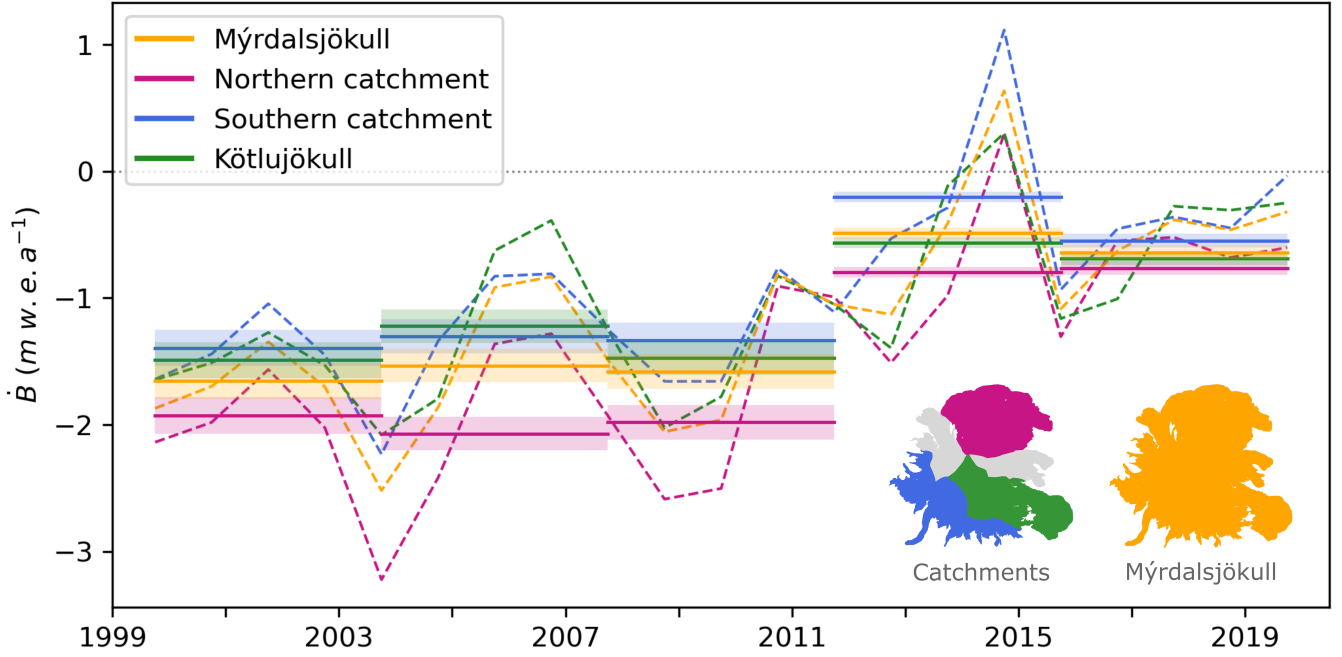


Fig. 12: Mass balance of glacierized catchments. Dashed lines represent annual mass balance values computed on hydrological years. Four-hydrological-year mass balance and the corresponding uncertainties are indicated with solid lines.

mostly like the entire Mýrdalsjökull. Both have very similar mass balance values that differ by a maximum of $0.31 \text{ m w.e. a}^{-1}$.

Despite climatic contrasts between the northern and southern areas of Mýrdalsjökull, no significant differences in terms of variability appear between the catchments. Exposed to a more continental and less fluctuating climate, the northern catchment could have been expected to experience less temporal variability than the southern one. However, the same variability is observed for the three catchments as for the whole ice cap.

Period	Myrdalsjökull \dot{B} (m w.e. a ⁻¹)	Northern catchment \dot{B}_N (m w.e. a ⁻¹)	Southern catchment \dot{B}_S (m w.e. a ⁻¹)	Kötlujökull \dot{B}_K (m w.e. a ⁻¹)
1999–2003	-1.65 ± 0.14	-1.93 ± 0.14	-1.39 ± 0.14	-1.49 ± 0.14
2003–2007	-1.53 ± 0.13	-2.07 ± 0.13	-1.30 ± 0.13	-1.22 ± 0.13
2007–2011	-1.58 ± 0.14	-1.98 ± 0.14	-1.33 ± 0.14	-1.47 ± 0.14
2011–2015	-0.49 ± 0.04	-0.80 ± 0.04	-0.20 ± 0.04	-0.56 ± 0.04
2015–2019	-0.64 ± 0.06	-0.76 ± 0.06	-0.55 ± 0.06	-0.69 ± 0.06

Table 2: Mass balance on 4-hydrological-year periods on Mýrdalsjökull and glacierized catchments.

4.4 Climate model results

Results on the ice cap. Over the studied time span, no clear trend can be identified neither in summer temperature nor in winter precipitation. Especially for normalized winter precipitation, variations are very marginal and range between 0.79 and 1.26 around the average value on 1999–2019 (Fig. 13a,b). As a consequence, the sensitivity to winter precipitation was at first negative when running the model. To keep the physical significance of the climatic model, the winter precipitation sensitivity ($\frac{\partial \dot{B}}{\partial P_w}$) was forced to $0 \text{ m w.e. a}^{-1}(10\%^{-1})$, meaning that the winter precipitation term was removed from Eq. (1). The results from this second version of the climatic model are shown in Fig. 13.

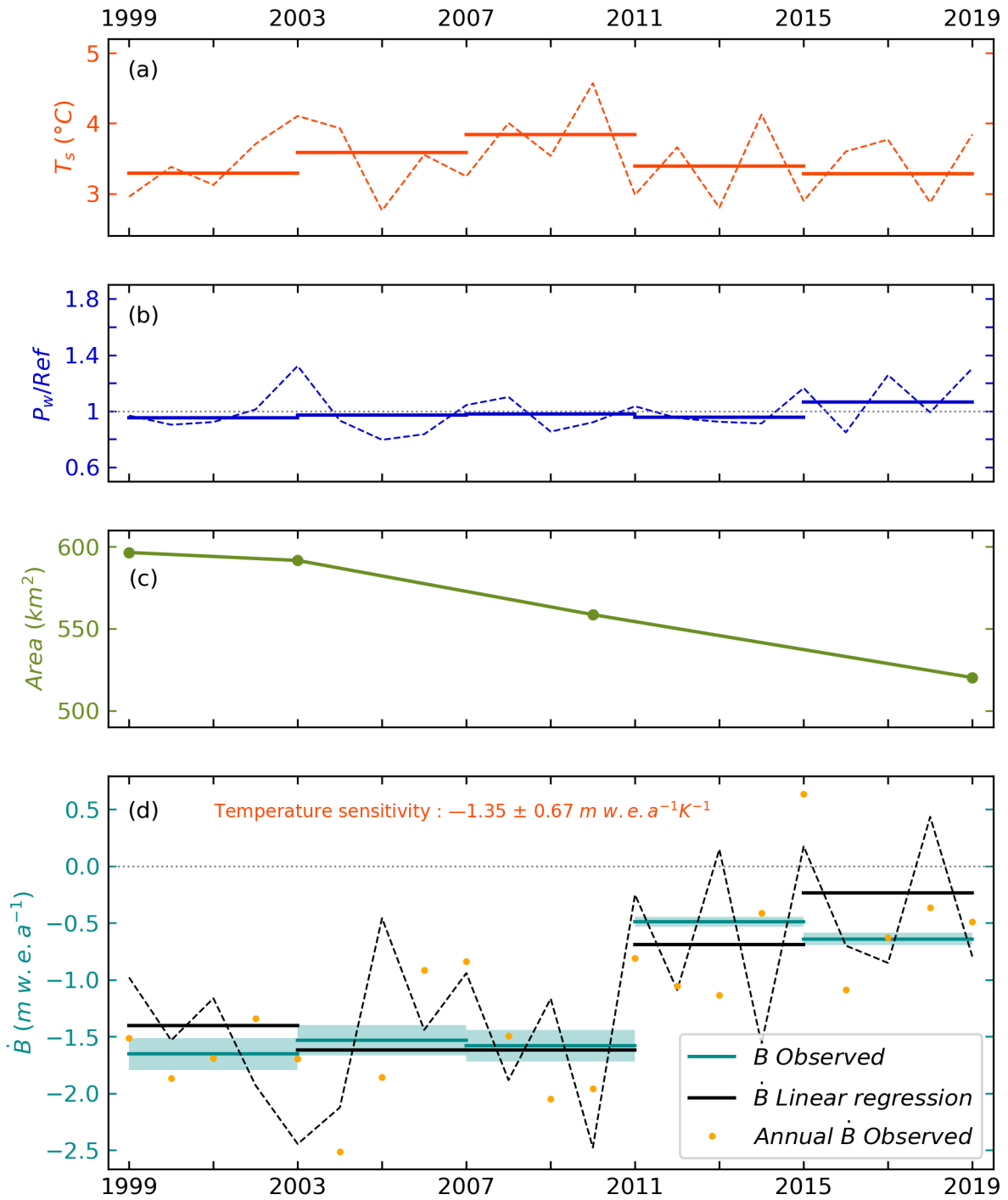


Fig. 13: Results of the climatic model on Mýrdalsjökull ice cap. **(a)** The dashed line represents the mean summer temperature at the ELA. Averages over four years are indicated in solid lines. **(b)** Annual normalized winter precipitation at the ELA (divided by the average 1999–2019) is shown in a dashed line. Solid lines represent the four-year averages. **(c)** The total glacierized area is linearly interpolated from reference areas calculated with the glaciers outlines in 1999, 2003, 2010 and 2019 (green dots). **(d)** Comparison between $\dot{B}_{observed}$ obtained with GP-generated DEMs and $\dot{B}_{linear\ regression}$ computed with the climatic model. Orange dots correspond to annual values of $\dot{B}_{observed}$ and four-year mass balance with their uncertainty are shown in blue. $\dot{B}_{linear\ regression}$ is indicated with solid black lines on the same four-year periods and with a dashed line for single years.

When comparing $\dot{B}_{observed}$ obtained with GP-generated DEMs and $\dot{B}_{linear\ regression}$ computed with the climatic model on four-year periods, the linear regression model both over and underestimates mass balance but reproduces quite accurately the general trend (Fig. 13d). With annual values, only the overall tendency can be explained by the model.

Results on the three catchments. Significant differences between the three catchments can be identified in terms of climate variables and climate model results (Fig. 14). First, the northern catchment has the highest summer temperatures and the smallest winter precipitation. It also shows the lowest temperature sensitivity (-1.17 ± 1.25 m w.e. $a^{-1}K^{-1}$). On the other hand, the southern catchment mostly behaves like the entire ice cap and presents a similar temperature sensitivity (-1.31 ± 0.88 m w.e. $a^{-1}K^{-1}$). In contrast, if summer temperatures are almost identical for Kötlujökull as for the whole ice cap, winter precipitations appear to be much more significant, at least 20% higher than the 1999–2019 average. The temperature sensitivity (-1.44 ± 0.31 m w.e. $a^{-1}K^{-1}$) is also the highest among the three catchments studied. Similarly to the results on the entire glacier, $\dot{B}_{linear\ regression}$ reproduces faithfully the overall trend but cannot capture the annual variability of the mass balance.

5 Discussion

5.1 Gaussian Process regression

The Gaussian Process regression is a cutting edge technique in DEM processing developed by Hugonnet et al. (2021). Thanks to the tools implemented in the github repository *pyddem*, it can be used easily through automated commands. This method improves many aspects of DEM analysis and mass balance computations. First, it allows to overcome the typical issue of spatial and temporal coverage common in geodetic mass balance studies (e.g. Fischer et al. (2015), Andreassen et al. (2016)). Multiple factors prevent the creation of complete series of non-voided DEMs on long time spans, such as cloud cover, sensors characteristics and data accessibility. The GP regression produces a temporally and spatially continuous dataset which enables computations over precise areas and time periods. Mass balance estimates can be calculated on specific dates, such as hydrological years, without requiring a seasonal correction for each DEM unlike many studies (e.g. Belart et al. (2020), Magnússon et al. (2016)).

Another advantage of this method is its robustness. The GP regression has been validated through a comparison between ICESat data and synthetic DEMs generated from ASTER and ArcticDEM data. An excellent agreement was found between the two datasets, enabling the validation of the method (Hugonnet et al., 2021). In our study, the comparison between a GP-generated DEM and the lidar DEM also shows a good agreement.

The data filtering included in the GP implementation in *pyddem* leads to much smoother maps and lower uncertainties in further calculations (Fig. 8, Fig. 11). The method was initially designed for processing ASTER and ArcticDEM data as part of a global analysis of glacier mass loss. To deal with very noisy and coarse resolution datasets, very efficient steps of observations filtering and weighting were developed. In our study, Pléiades and SPOT5 high resolution imagery were processed in order to investigate a comparatively small glacier. Therefore, the GP regression could be applied to those datasets with high confidence.

Although it brings substantial improvements in DEM treatment, the GP method presents some limitations. First, the GP regression shows difficulty in capturing annual and seasonal trends. This is quite clear on the elevation time series extracted at specific locations of the glacier from Fig. 10, as the 1σ interval remains large around seasonal variations. Then, the GP regression produces a general smoothing of elevation changes, especially when data are missing. For example, the elevation drop in 2010 related to the Eyjafjallajökull eruption is indeed rather accurately reproduced. Over the period 2008-07-09 to 2010-08-09, very similar mass balance rates are obtained with survey date and with GP-based elevation difference maps, -2.85 ± 0.14 m w.e. a^{-1} and -2.68 ± 0.23 m w.e. a^{-1} respectively (Fig. 11a). However, the Gaussian Process regression extrapolates this low value observed in 2010 to the year 2009 as no DEM is available to fit data with (data temporal distribution on Fig. 2c). Such

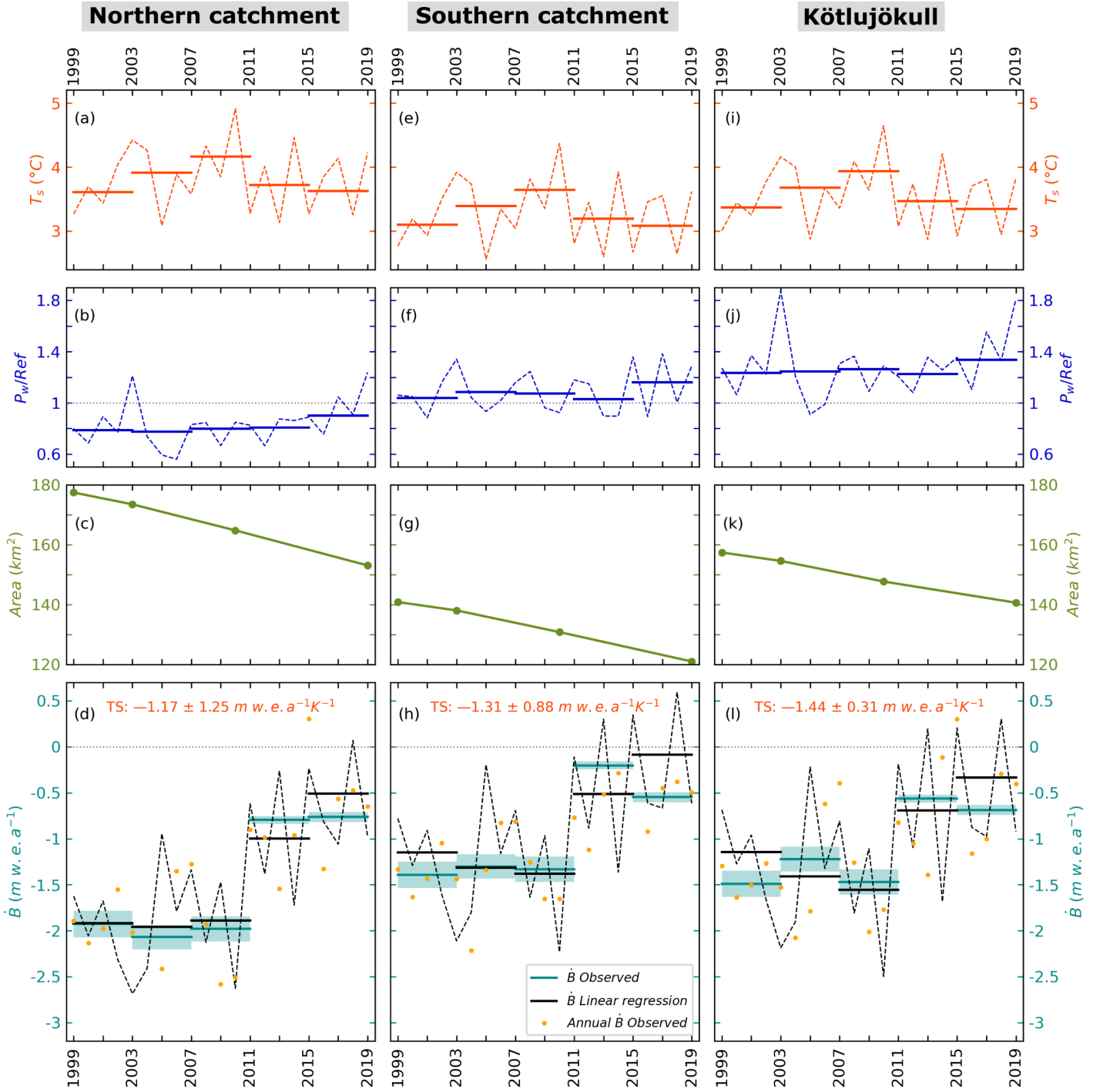


Fig. 14: Results of the climatic model on the three catchments. (a), (e), (i) The dashed line represents the mean summer temperature at the ELA. Averages over four years are indicated in solid lines. (b), (f), (j) Annual normalized winter precipitation at the ELA (divided by the average 1999–2019) is shown in a dashed line. Solid lines represent the four-year averages. (c), (g), (k) Glacierized areas are linearly interpolated from reference areas calculated with the catchments outlines in 1999, 2003, 2010 and 2019 (green dots). (d), (h), (i) Comparison between $\dot{B}_{observed}$ obtained with GP-generated DEMs and $\dot{B}_{linear\ regression}$ computed with the climatic model. Orange dots correspond to annual values of $\dot{B}_{observed}$ and four-year mass balance with their uncertainty are shown in blue. $\dot{B}_{linear\ regression}$ is indicated with solid black lines on the same four-year periods and with a dashed line for single years.

a negative mass balance is not expected for 2009 as no particular climatic or volcanic event has been recorded. Therefore, using synthetic DEMs generated with the GP regression requires caution: when data are missing, the GP can only offer a logical temporal interpolation of existing values that follows the general elevation change tendency.

An adaptation of the kernels used in the GP could have been considered to better account for the conditions of Mýrdalsjökull. For example, the model of variance could be changed to more accurately take into account the exceptional melting in the summer 2010 following the Eyjafjallajökull eruption. However a more sensitive kernel could also affect and overfit the beginning and end of the elevation time series, where the data is scarce.

5.2 Mass balance

5.2.1 Annual mass balance and conversion factor

Annual mass balance values were computed in this study. They are useful to have a temporally detailed dataset, for example to compare with in situ observations (Fig. 15) or to evaluate the prediction capacities of a model (Fig. 13). Nevertheless, the limited amount of data does not enable the calculation of very accurate annual mass balance. Huss (2013) investigates the robustness of the conversion factor $f_{\Delta V}$. As firn density profile is continually evolving with accumulation and melting events, assuming a constant value valid for all situations is not easy, especially in short periods (<4 years).

However, even if the conversion factor is not robust over short time periods, considering annual mass balance values can help to identify short-term variations or patterns. When larger periods are studied, a trustable long-term trend can be found but it smoothes all the short-term variability. In addition, there are many ways to try to reduce the limitations of the conversion factor estimate. First, larger uncertainties can be added when working on shorter periods. Then, in situ density measurement (Ágústsson et al., 2013) could be used to adapt the conversion factor $f_{\Delta V}$.

5.2.2 Comparison with other studies

Comparison with global results. To put the geodetic mass balance results obtained for Mýrdalsjökull ice cap in this study in a broader context, estimates for other glaciers on similar time periods were extracted. Mass balance from Zemp et al. (2019) ranged from -0.03 ± 0.12 to -1.18 ± 0.38 m w.e. a^{-1} (South Asia West and Southern Andes respectively) between 2006 and 2016. For Iceland, estimates were rather close to the lower values worldwide (-0.71 ± 0.43 m w.e. a^{-1}). According to our results, Mýrdalsjökull mass loss appeared to be even more negative for the decade 2004–2014 with a mass balance rate of -1.24 ± 0.12 m w.e. a^{-1} . Hugonnet et al. (2021) obtained mass balance of -0.88 ± 0.13 m w.e. a^{-1} over the two decades 1999–2019 in Iceland, lower than those of the southern Arctic region (encompassing Alaska, Arctic Canada South, southern Greenland Periphery, Iceland and Scandinavia) of -0.74 ± 0.10 m w.e. a^{-1} . Again, our study led to more negative estimates for Mýrdalsjökull, especially in the first decade (-1.62 ± 0.14 m w.e. a^{-1} between 1999 and 2009). Similarly, the mass balance obtained in Aðalgeirsdóttir et al. (2020) over the period 2006–2018 (-7.6 ± 0.8 Gt $\cdot a^{-1}$) corresponding to an average mass balance rate of -0.69 ± 0.07 m w.e. a^{-1} for all Icelandic glaciers, was less negative than our estimates for Mýrdalsjökull. Mass balance results from Belart et al. (2020) (-2.40 ± 0.25 m w.e. a^{-1} between 1999 and 2004, -1.74 ± 0.17 m w.e. a^{-1} between 2004 and 2010 and -0.30 ± 0.12 m w.e. a^{-1} between 2010 and 2016) showed a good agreement with the results of our study.

Thus, Mýrdalsjökull ice cap presented very negative mass balance rates when compared to other Icelandic glaciers or to other glacierized regions worldwide. This could be explained by the local conditions of the ice cap, characterized by a low elevation range and a high sensitivity to temperature changes. The proximity of Mýrdalsjökull to the South coast of Iceland and the warm Irminger current could also account for this extremely high mass loss over the past two decades.

Comparison with glaciological mass balance from other Icelandic ice caps. Mean specific surface mass balance records were extracted from Aðalgeirsdóttir et al. (2020) for the three largest Icelandic ice caps. Thanks to regular in situ surveys, winter and summer mass balance have been

collected every year since 1991/92, 1987/88, 1996/97 for Vatnajökull (~ 60 locations), Hofsjökull (~ 25 locations) and Langjökull (~ 25 locations), respectively. Those datasets were then used to compute annual specific surface mass balance. However, as detailed in Jóhannesson et al. (2020), specific surface mass balance does not take into account non-surface phenomena including volcanic eruptions, geothermal melting, calving and energy dissipation in the ice motion and at the basal interface. As a consequence, it can differ from estimates produced with geodetic measurements, up to 10% of the measurements. Some physical phenomena can be considered negligible to a certain extent, such as calving for Hofsjökull and Langjökull. Nevertheless, when compared with geodetic results obtained from DEMs analysis, Hofsjökull surface mass balance appeared to be biased and was subsequently corrected. Therefore the existence of a potential bias requires caution when using specific surface mass balance values.

Annual mass balance surveys have also been conducted on Mýrdalsjökull since 2007 at three locations (Ágústsson et al., 2013). Yet, because of the scarcity of measurement sites, heavily skewed in the accumulation area, it is not possible to infer mass balance estimates for the whole ice cap. Obtaining a reliable estimate of specific surface mass balance based on the in situ observations is therefore not possible for Mýrdalsjökull.

Fig. 15a shows the geodetic annual mass balance rates of Mýrdalsjökull (from GP-based) DEMs and the glaciological mass balance (based on in situ observations) of Vatnajökull, Hofsjökull and Langjökull (Aðalgeirsdóttir et al., 2020). The general mass balance trend is similar for all four glaciers. First, there is a gradual decrease in mass loss during one and a half decades starting in the early 2000s. This tendency comes to an end in 2015, when the mass balance reaches a positive value. After 2015, an increasing trend of mass loss is observed until the end of the records. Over the study period, Mýrdalsjökull geodetic mass balance rates fluctuate from -2.07 to $+0.68$ m w.e. a^{-1} . They are distributed in the same range as the other ice caps mass balance rates, which spread from -2.01 to $+0.78$ m w.e. a^{-1} for Vatnajökull, from -3.10 to $+0.84$ m w.e. a^{-1} for Hofsjökull and from -3.80 to $+0.41$ m w.e. a^{-1} for Langjökull.

The four ice caps also present similarities in terms of temporal variability. One-time events induce comparable consequences on the glaciers. The Eyjafjallajökull eruption in 2010 leads to extremely negative mass balance rates for Vatnajökull (-2.01 m w.e. a^{-1}), Langjökull (-3.10 m w.e. a^{-1}) and Hofsjökull (-3.80 m w.e. a^{-1}). This effect is also clearly visible on Mýrdalsjökull in 2010 (-2.06 m w.e. a^{-1}) despite the GP-artefact caused by the lack of data in 2009 (-2.07 m w.e. a^{-1}). Likewise, the four ice caps all present positive annual mass balances in 2014 – 2015 related to a climatic anomaly, also observed in Hugonnet et al. (2021). Eventually, the standard deviations computed on the period 2000–2021 are in the same range for Vatnajökull, Langjökull, Hofsjökull and Mýrdalsjökull, 0.56, 0.86, 0.76 and 0.76 m w.e. a^{-1} , respectively.

In order to further examine the statistical relationships between Mýrdalsjökull and the three largest ice caps, correlations between mass balance values were computed. The corresponding scatter plots are shown in Fig. 15b, c and d. It appears that the correlation coefficients are rather low and no significant correlation can be identified.

5.2.3 Mass balance at the different catchments

Because of climatic disparities between the northern and southern outlets of Mýrdalsjökull, differences in mass balance variability can be expected. As the South area receives a large amount of precipitation, it could be more sensitive to snowfall and rainfall fluctuations and therefore show more variations with time (Björnsson and Pálsson, 2008; Crochet, 2007). This was observed by Belart et al. (2020) when comparing mass balance rates between decades. The southern catchment of Mýrdalsjökull showed significant mass gain between 1960 and 1984 followed by a strong retreat from 1984 to 2010. Conversely, northern outlets experienced an overall declining trend over the 5 decades. However, in our study, focusing on a narrow time period of two decades, larger variability is not observed in the southern catchment (Fig. 8). In the past two decades, the northern and the southern halves of Mýrdalsjökull have shown similar mass balance variations since 2000. The variability related to climate of South Mýrdalsjökull could require a longer study period in order to be observed. In other words,

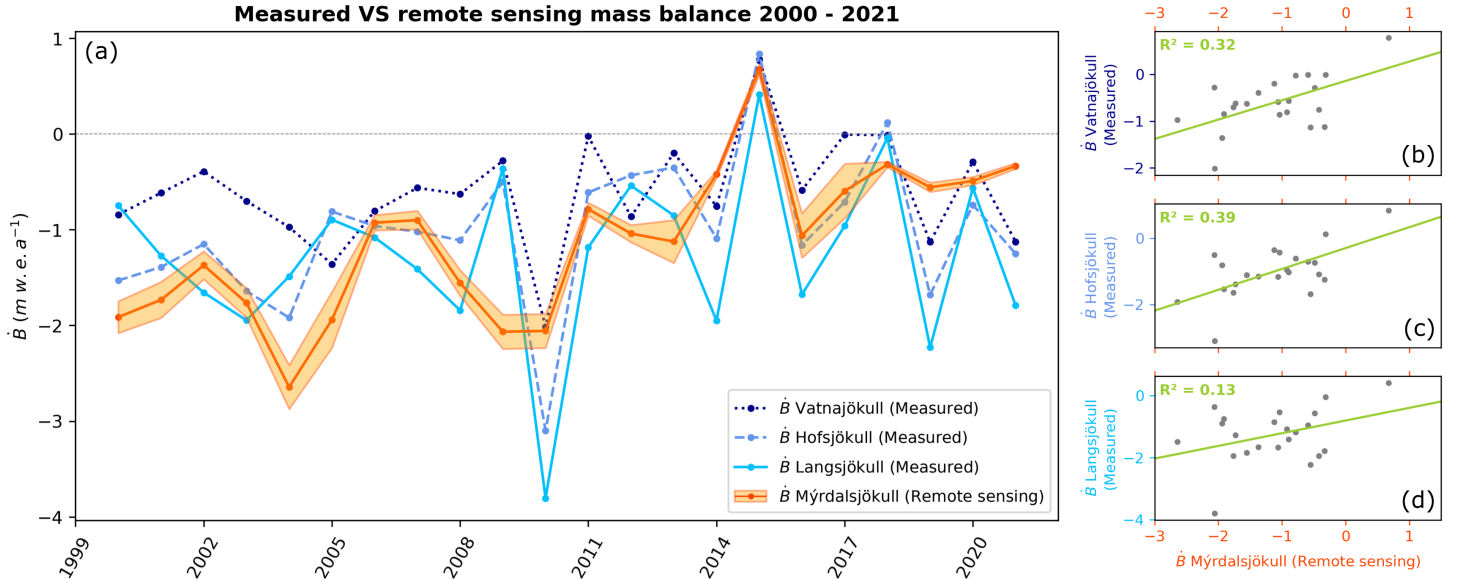


Fig. 15: Geodetic vs glaciological mass balance, 2000–2021. **(a)** Comparison between measured specific surface mass balance of the three largest Icelandic ice caps and geodetic annual mass balance of Mýrdalsjökull. Corresponding correlations are shown in the right panels: **(b)** for Vatnajökull, **(c)** for Hofsjökull and **(d)** for Langsjökull.

longer periods of climate variation could be needed to detect different statistical characteristics of the southern and northern outlets.

5.3 Joint analysis of mass balance and climate

5.3.1 Climatic sensitivities

Due to small variations of winter precipitation over the past two decades, the sensitivity to this climate variable is forced to 0 m w.e. a⁻¹(10%⁻¹). The short-term response of Mýrdalsjökull ice cap thus appears to be mainly related to summer temperature changes (Fig. 13). The computed temperature sensitivities (−1.35 m w.e. a⁻¹K⁻¹ for the entire ice cap, −1.31, −1.17 and −1.44 m w.e. a⁻¹K⁻¹ for the southern catchment, northern catchment and Kötlujökull, respectively) are within the expected range of values for maritime glaciers (De Woul and Hock, 2005). Belart et al. (2019) obtained a comparable temperature sensitivity (−2.5 m w.e. a⁻¹K⁻¹) for the neighbour glacier Eyjafjallajökull, as well as De Woul and Hock (2005) for selected catchments of Vatnajökull and Hofsjökull (−0.8 to −2.0 m w.e. a⁻¹K⁻¹).

The short time period of this study leads to difficulties in constraining sensitivities as a limited number of values is available. Therefore, climate sensitivity computation might require longer periods to get more robust results as in Belart et al. (2020) and Engelhardt et al. (2015). Climate variations are more likely to impact glacier mass balance when several decades are considered, as time is required for ice caps to adapt to varying conditions. Response of glaciers to climate variability is indeed often longer than a few years or a decade. This also reminds of the need for long-term studies that go further back in time as Belart et al. (2020). A comparison between long-term and short-term sensitivities could still be of interest, reflecting different time scales of glacier response to climate changes.

5.3.2 Linear model limitations

In this study, climate variables associated with a surface correction term can explain a large part of the mass balance variability. The mass balance predictions on four-year periods are in agreement with the original estimates and the general trend of annual predictions is correct. However, this model offers a simplified interpretation of the relationship between mass balance and climate variables. First,

other physical processes affecting mass balance such as albedo changes could be taken into account (e.g. Gunnarsson et al. (2021)). This can influence mass balance estimates in the event of ash falls or summer snowfall, which are frequent on Mýrdalsjökull (e.g. Gudmundsson et al. (2012)). Other phenomena could also be included in more complex models. For example, the surface-correction term could be more precisely specified and basal and internal melting explicitly accounted for.

6 Conclusion

This study presents geodetic mass balance estimates of Mýrdalsjökull ice cap over the past two decades 1999–2019 based on Pléiades, SPOT5, lidar, aerial photogrammetry and ArcticDEM datasets. The Gaussian Process regression, cutting edge method in DEM processing, was applied to pre-processed data in order to generate a continuous dataset of synthetic DEMs with a spatial resolution of 15 m x 15 m and temporal resolution of 30 days. The latter was thereafter used for geodetic mass balance computation on hydrological years (October 1st–September 31st). The obtained mass balance become progressively less negative over the two decades, from -1.82 ± 0.16 m w.e. a⁻¹ (1999–2004) to -0.39 ± 0.03 m w.e. a⁻¹ (2014–2019). However, the mass balance becomes more negative again after 2017.

Three catchments were delineated and analysed in order to identify local patterns of mass balance. The northern catchment appeared to present the highest mass loss, whereas Kötlujökull behaved in a very similar manner as the entire ice cap. No difference in mass balance variability was observed between the three catchments over the two decades.

A joint analysis of mass balance and climate was performed in order to characterize Mýrdalsjökull response to climatic changes over the two decades. A high mass balance sensitivity to temperature changes (-1.35 m w.e. a⁻¹K⁻¹) was obtained, in agreement with values for other maritime glaciers. However, longer study time periods and more complex models would be required to compute more robust mass balance sensitivities to climate changes.

Acknowledgments

I would like to thank Andri Gunnarsson for all the logistics of my internship and the Landsvirkjun for funding my research at the University of Iceland. I thank Etienne Berthier for having introduced me to the Icelandic research group and for having followed my work until the end with many useful and interesting comments and ideas. I also thank Romain Hugonnet and Amaury Dehecq for answering my numerous emails (always so quickly!) and helping me in my struggle against all the coding problems. I acknowledge Romain Hugonnet and Gaston Bidou for having taken the time to read my thesis. I thank Tómas Jóhannesson, Finnur Pálsson and Eyjolfur Magnusson for their help and for the various discussions we had about Iceland, including the sheep's stomach. I am grateful to the Icelandic Glaciological Society for having organised the spring trip on Vatnajökull, one of the most memorable experiences of my time in Iceland.

Eventually, I thank Joaquín MC Belart for being a really nice supervisor, always available and enthusiastic about "mettre les mains dans le cambouis" to help me, but also always ready to talk about various things, from blacksmithing to Irish music. Thanks for having made this internship a fantastic experience!

Pléiades images were acquired at research price thanks to the CNES ISIS programme (<http://www.isis-cnes.fr>). This study uses the lidar mapping of the glaciers in Iceland, funded by the Icelandic Research Fund, the Landsvirkjun research fund, the Icelandic Road Administration, the Reykjavík Energy Environmental and Energy Research Fund, the Klima- og Luftgruppen research fund of the Nordic Council of Ministers, the Vatnajökull National Park, the organization Friends of Vatnajökull, LMÍ, IMO, and the UI research fund.

References

- Aðalgeirsdóttir, G., Jóhannesson, T., Björnsson, H., Pálsson, F., and Sigurðsson, O. (2006). Response of Hofsjökull and southern Vatnajökull, Iceland, to climate change. *Journal of Geophysical Research: Earth Surface*, 111(F3).
- Aðalgeirsdóttir, G., Magnússon, E., Pálsson, F., Thorsteinsson, T., Belart, J. M., Jóhannesson, T., Hannesdóttir, H., Sigurðsson, O., Gunnarsson, A., Einarsson, B., et al. (2020). Glacier changes in Iceland from 1890 to 2019. *Frontiers in Earth Science*, 8:523646.
- Ágústsson, H., Hannesdóttir, H., Þorsteinsson, Þ., Pálsson, F., Oddsson, B., and Ólafsson, H. (2013). Mass balance of Myrdalsjökull ice cap and comparison with observed and simulated precipitation. page 13302.
- Andreassen, L. M., Elvehøy, H., Kjølmoen, B., and Engeset, R. V. (2016). Reanalysis of long-term series of glaciological and geodetic mass balance for 10 Norwegian glaciers. *The Cryosphere*, 10(2):535–552.
- Belart, J., Magnússon, E., Berthier, E., Gunnlaugsson, Á. Þ., Pálsson, F., Aðalgeirsdóttir, G., Jóhannesson, T., Thorsteinsson, T., and Björnsson, H. (2020). Mass balance of 14 Icelandic glaciers, 1945–2017: spatial variations and links with climate. *Frontiers in Earth Science*, page 163.
- Belart, J. M., Magnússon, E., Berthier, E., Pálsson, F., Aðalgeirsdóttir, G., and Jóhannesson, T. (2019). The geodetic mass balance of Eyjafjallajökull ice cap for 1945–2014: processing guidelines and relation to climate. *Journal of Glaciology*, 65(251):395–409.
- Bengtsson, L., Andrae, U., Aspelien, T., Batrak, Y., Calvo, J., de Rooy, W., Gleeson, E., Hansen-Sass, B., Homleid, M., Hortal, M., et al. (2017). The HARMONIE--AROME model configuration in the ALADIN–HIRLAM NWP system. *Monthly Weather Review*, 145(5):1919–1935.
- Berthier, E., Cabot, V., Vincent, C., and Six, D. (2016). Decadal region-wide and glacier-wide mass balances derived from multi-temporal ASTER satellite digital elevation models. Validation over the Mont-Blanc area. *Frontiers in Earth Science*, 4:63.
- Berthier, E., Vincent, C., Magnússon, E., Gunnlaugsson, Á., Pitte, P., Le Meur, E., Masiokas, M., Ruiz, L., Pálsson, F., Belart, J., et al. (2014). Glacier topography and elevation changes derived from Pléiades sub-meter stereo images. *The Cryosphere*, 8(6):2275–2291.
- Björnsson, H. and Pálsson, F. (2008). Icelandic glaciers. *Jökull*, 58(58):365–386.
- Björnsson, H., Pálsson, F., and Guðmundsson, M. T. (2000). Surface and bedrock topography of the Myrdalsjökull ice cap. *Jökull*, 49:29–46.
- Brun, F., Berthier, E., Wagnon, P., Kääb, A., and Treichler, D. (2017). A spatially resolved estimate of High Mountain Asia glacier mass balances from 2000 to 2016. *Nature geoscience*, 10(9):668–673.
- Cogley, J. G. (2011). Present and future states of Himalaya and Karakoram glaciers. *Annals of Glaciology*, 52(59):69–73.
- Consortium, R. (2017). Randolph Glacier Inventory - A dataset of Global Glacier Outlines, version 6.
- Crochet, P. (2007). A study of regional precipitation trends in Iceland using a high-quality gauge network and ERA-40. *Journal of Climate*, 20(18):4659–4677.
- Crochet, P. and Jóhannesson, T. (2011). A dataset of daily temperature in Iceland for the period 1949–2010. *Jökull 2011: 1*, 61.
- De Woul, M. and Hock, R. (2005). Static mass-balance sensitivity of Arctic glaciers and ice caps using a degree-day approach. *Annals of Glaciology*, 42:217–224.

- Dehecq, A., Gardner, A. S., Alexandrov, O., McMichael, S., Hugonnet, R., Shean, D., and Marty, M. (2020). Automated processing of declassified KH-9 Hexagon satellite images for global elevation change analysis since the 1970s. *Frontiers in Earth Science*, 8:566802.
- Deschamps-Berger, C. (2021). *Apport de la photogrammétrie satellite pour la modélisation du manteau neigeux*. PhD thesis, Université Paul Sabatier-Toulouse III.
- Dussaillant, I., Berthier, E., Brun, F., Masiokas, M., Hugonnet, R., Favier, V., Rabatel, A., Pitte, P., and Ruiz, L. (2019). Two decades of glacier mass loss along the Andes. *Nature Geoscience*, 12(10):802–808.
- Engelhardt, M., Schuler, T. V., and Andreassen, L. M. (2015). Sensitivities of glacier mass balance and runoff to climate perturbations in Norway. *Annals of Glaciology*, 56(70):79–88.
- Fischer, M., Huss, M., and Hoelzle, M. (2015). Surface elevation and mass changes of all Swiss glaciers 1980–2010. *The Cryosphere*, 9(2):525–540.
- Girod, L., Nuth, C., Kääb, A., McNabb, R., and Galland, O. (2017). MMASTER: improved ASTER DEMs for elevation change monitoring. *Remote Sensing*, 9(7):704.
- Gudmundsson, M. T., Larsen, G., Höskuldsson, Á., and Gylfason, Á. G. (2008). Volcanic hazards in Iceland. *Jökull*, 58:251–268.
- Gudmundsson, M. T., Thordarson, T., Höskuldsson, Á., Larsen, G., Björnsson, H., Prata, F. J., Oddsson, B., Magnússon, E., Högnadóttir, T., Petersen, G. N., et al. (2012). Ash generation and distribution from the April-May 2010 eruption of Eyjafjallajökull, Iceland. *Scientific reports*, 2(1):1–12.
- Gunnarsson, A., Gardarsson, S. M., Pálsson, F., Jóhannesson, T., and Sveinsson, Ó. G. (2021). Annual and inter-annual variability and trends of albedo of Icelandic glaciers. *The Cryosphere*, 15(2):547–570.
- Hannesdóttir, H., Björnsson, H., Pálsson, F., Aðalgeirsdóttir, G., and Guðmundsson, S. (2015). Changes in the southeast Vatnajökull ice cap, Iceland, between 1890 and 2010. *The Cryosphere*, 9(2):565–585.
- Hannesdóttir, H., Sigurðsson, O., Þrastarson, R. H., Guðmundsson, S., Belart, J. M., Pálsson, F., Magnússon, E., Víkingsson, S., Kaldal, I., and Jóhannesson, T. (2020). A national glacier inventory and variations in glacier extent in Iceland from the Little Ice Age maximum to 2019. *Jökull 2020: 1*, 34.
- Höhle, J. and Höhle, M. (2009). Accuracy assessment of digital elevation models by means of robust statistical methods. *ISPRS Journal of Photogrammetry and Remote Sensing*, 64(4):398–406.
- Hugonnet, R., Brun, F., Berthier, E., Dehecq, A., Mannerfelt, E. S., Eckert, N., and Farinotti, D. (2022). Uncertainty analysis of digital elevation models by spatial inference from stable terrain. *IEEE Journal of Selected Topics in Applied Earth Observations and Remote Sensing*.
- Hugonnet, R., McNabb, R., Berthier, E., Menounos, B., Nuth, C., Girod, L., Farinotti, D., Huss, M., Dussaillant, I., Brun, F., et al. (2021). Accelerated global glacier mass loss in the early twenty-first century. *Nature*, 592(7856):726–731.
- Huss, M. (2013). Density assumptions for converting geodetic glacier volume change to mass change. *The Cryosphere*, 7(3):877–887.
- Huss, M. and Farinotti, D. (2012). Distributed ice thickness and volume of all glaciers around the globe. *Journal of Geophysical Research: Earth Surface*, 117(F4).

- Johannesson, T., Björnsson, H., Magnusson, E., Guðmundsson, S., Pálsson, F., Sigurðsson, O., Thorsteinsson, T., and Berthier, E. (2013). Ice-volume changes, bias estimation of mass-balance measurements and changes in subglacial lakes derived by lidar mapping of the surface of Icelandic glaciers. *Annals of Glaciology*, 54(63):63–74.
- Jóhannesson, T., Björnsson, H., Pálsson, F., Sigurðsson, O., and Þorsteinsson, Þ. (2011). LiDAR mapping of the Snæfellsjökull ice cap, western Iceland. *Jökull*, 61:19–32.
- Jóhannesson, T., Pálmason, B., Hjartarson, Á., Jarosch, A. H., Magnússon, E., Belart, J. M., and Guðmundsson, M. T. (2020). Non-surface mass balance of glaciers in Iceland. *Journal of Glaciology*, 66(258):685–697.
- Korona, J., Berthier, E., Bernard, M., Rémy, F., and Thouvenot, E. (2009). SPIRIT. SPOT 5 stereoscopic survey of polar ice: reference images and topographies during the fourth International Polar Year (2007–2009). *ISPRS journal of photogrammetry and remote sensing*, 64(2):204–212.
- Magnússon, E., Muñoz-Cobo Belart, J., Pálsson, F., Ágústsson, H., and Crochet, P. (2016). Geodetic mass balance record with rigorous uncertainty estimates deduced from aerial photographs and lidar data—Case study from Drangajökull ice cap, NW Iceland. *The Cryosphere*, 10(1):159–177.
- Magnússon, E., Pálsson, F., Jarosch, A. H., van Boeckel, T., Hannesdóttir, H., and Belart, J. M. (2021). The bedrock and tephra layer topography within the glacier filled Katla caldera, Iceland, deduced from dense RES-survey. *JOKULL*, (71):39–70.
- McNabb, R., Nuth, C., Kääh, A., and Girod, L. (2019). Sensitivity of glacier volume change estimation to DEM void interpolation. *The Cryosphere*, 13(3):895–910.
- Nawri, N., Pálmason, B., Petersen, G. N., Björnsson, H., and Þorsteinsson, S. (2017). The ICRA atmospheric reanalysis project for Iceland. *Icel Meteorol Off*, 5.
- Nuth, C. and Kääh, A. (2011). Co-registration and bias corrections of satellite elevation data sets for quantifying glacier thickness change. *The Cryosphere*, 5(1):271–290.
- Pálsson, F., Guðmundsson, S., Björnsson, H., Berthier, E., Magnússon, E., Guðmundsson, S., and Haraldsson, H. H. (2012). Mass and volume changes of Langjökull ice cap, Iceland, 1890 to 2009, deduced from old maps, satellite images and in situ mass balance measurements. *Jökull*, 62(2012):81–96.
- Porter, C., Morin, P., Howat, I., Noh, M., Bates, B., Peterman, K., Keeseey, S., Schlenk, M., Gardiner, J., et al. (2018). Arctic DEM. *Harvard Dataverse*, 1.
- Rolstad, C., Haug, T., and Denby, B. (2009). Spatially integrated geodetic glacier mass balance and its uncertainty based on geostatistical analysis: application to the western Svartisen ice cap, Norway. *Journal of Glaciology*, 55(192):666–680.
- Shean, D. E., Alexandrov, O., Moratto, Z. M., Smith, B. E., Joughin, I. R., Porter, C., and Morin, P. (2016). An automated, open-source pipeline for mass production of digital elevation models (DEMs) from very-high-resolution commercial stereo satellite imagery. *ISPRS Journal of Photogrammetry and Remote Sensing*, 116:101–117.
- Williams, C. K. and Rasmussen, C. E. (2006). *Gaussian processes for machine learning*, volume 2. MIT press Cambridge, MA.
- Zemp, M., Huss, M., Thibert, E., Eckert, N., McNabb, R., Huber, J., Barandun, M., Machguth, H., Nussbaumer, S. U., Gärtner-Roer, I., et al. (2019). Global glacier mass changes and their contributions to sea-level rise from 1961 to 2016. *Nature*, 568(7752):382–386.